SÃO PAULO STATE UNIVERSITY
"JÚLIO DE MESQUITA FILHO"
SCHOOL OF ENGINEERING, SÃO JOÃO DA BOA VISTA

JOÃO PEDRO INNOCENTE GOSMIN

Quantification of Nonlinear Distortion in Optical Links Based on the 400ZR Standard

São João da Boa Vista
2025

João Pedro Innocente Gosmin

Quantification of Nonlinear Distortion in Optical Links Based on the 400ZR Standard

Undergraduate thesis presented to the Undergraduate Course Council in Electronic and Telecommunication Engineering of the School of Engineering in São João da Boa Vista, São Paulo State University, as part of the requirements for obtaining the Bachelor of Science degree in Electronic and Telecommunication Engineering.

Advisor: Prof. Ivan Aritz Aldaya Garde, PhD

São João da Boa Vista
2025

G676q

Gosmin, João Pedro Innocente
Quantification of nonlinear distortion in optical links based on the 400ZR standard / João Pedro Innocente Gosmin. -- São João da Boa Vista, 2025
57 p. : il., tabs.

Trabalho de conclusão de curso (Bacharelado - Engenharia de Telecomunicações) - Universidade Estadual Paulista (UNESP), Faculdade de Engenharia, São João da Boa Vista
Orientador: Ivan Aritz Aldaya Garde

1. Comunicações ópticas. 2. Engenharia. 3. Ótica não linear. 4. Telecomunicações. I. Título.

Sistema de geração automática de fichas catalográficas da Unesp. Dados fornecidos pelo autor(a).

UNIVERSIDADE ESTADUAL PAULISTA “JÚLIO DE MESQUITA FILHO”
FACULDADE DE ENGENHARIA - CÂMPUS DE SÃO JOÃO DA BOA VISTA
GRADUAÇÃO EM ENGENHARIA ELETRÔNICA E DE TELECOMUNICAÇÕES

TRABALHO DE CONCLUSÃO DE CURSO

QUANTIFICAÇÃO DA DISTORÇÃO NÃO LINEAR EM ENLACES ÓPTICOS COM PADRÃO 400 ZR

Aluno: João Pedro Innocente Gosmin
Orientador: Prof. Dr. Ivan Aritz Aldaya Garde

Banca Examinadora:

- Ivan Aritz Aldaya Garde (Orientador)
- Marlon Rodrigues Garcia (Examinador)
- Renata Mataveli Viti (Examinadora)

Os formulários de avaliação e a ata da defesa, na qual consta a aprovação do trabalho, devidamente assinados pela banca encontram-se no prontuário eletrônico do aluno.

São João da Boa Vista, 04 de dezembro de 2025

ACKNOWLEDGEMENTS

To my parents and my brother, for their support, encouragement, and unwavering assistance throughout every stage of my academic journey. To the faculty of UNESP – São João da Boa Vista Campus for all the support, knowledge, and resources provided for the development of this work. In particular, to my advisor, Ivan Aritz Aldaya Garde, for his trust and guidance since the beginning of my undergraduate research projects and throughout this final dissertation, and to Professor Rita de Cassia Domingos for her supervision during my earlier research activities. To my friends and colleagues who, in many different ways, contributed to this work—whether through ideas, emotional support, or companionship during my undergraduate years.

ABSTRACT

Coherent optical systems have transformed modern networks by enabling high transmission rates with elevated spectral efficiency, becoming increasingly common in short- and medium-reach links such as those defined by the 400 Gb/s coherent optical interface standard (400ZR) standard. These systems rely on coherent reception and intensive Digital Signal Processing (DSP) processing to compensate for linear effects, but they remain limited by noise accumulation—primarily amplified spontaneous emission (ASE) noise from optical amplifiers—as well as by fiber nonlinearities such as self-phase modulation (SPM), cross-phase modulation (XPM), and four-wave mixing (FWM), which distort the constellation and reduce the optical signal-to-noise ratio (OSNR) margin.
This work investigates, through a simulator fully developed in Python, the combined impact of these impairments on the performance of 400ZR-compliant systems, evaluating the evolution of the constellations, symbol-to-symbol interactions, distortion propagation, and the resulting penalties in bit-error-rate performance. The results show that, even in short-reach scenarios, nonlinear effects significantly influence the high-power regime, limiting the achievable reach and highlighting the need for effective compensation strategies. The analyses provided contribute to a deeper understanding of the operational limits of 400ZR links and offer essential insights for improving mitigation techniques applicable to future higher-capacity coherent interfaces.

KEYWORDS: coherent systems; 400ZR; nonlinear effects; DSP; optical simulation.

RESUMO

Os sistemas transformaram as redes modernas ao permitir altas taxas de transmissão com elevada eficiência espectral, tornando-se cada vez mais comuns em enlaces de curta e média distância, como aqueles definidos pelo padrão 400ZR. Esses sistemas utilizam recepção coerente e intenso DSP para compensar efeitos lineares, mas continuam limitados pela acumulação de ruído — principalmente ASE proveniente de amplificadores ópticos — e pelas não linearidades da fibra, como SPM, XPM e FWM, que distorcem a constelação e reduzem a margem de OSNR.
Este trabalho investiga, por meio de um simulador desenvolvido integralmente em Python, o impacto conjunto desses efeitos no desempenho de sistemas padronizados em 400ZR, avaliando a evolução das constelações, a interação entre símbolos, a propagação das distorções e as penalidades observadas na taxa de erro de bit. Os resultados mostram que, mesmo em enlaces curtos, as não linearidades influenciam significativamente o regime de alta potência, restringindo o alcance e evidenciando a necessidade de estratégias eficazes de compensação. As análises obtidas contribuem para o entendimento dos limites operacionais do 400ZR e oferecem informações essenciais para o aprimoramento de técnicas de mitigação aplicáveis às futuras interfaces coerentes de maior capacidade.

PALAVRAS-CHAVE: sistemas coerentes; 400ZR; efeitos não lineares; DSP; simulação óptica.

LIST OF FIGURES

LIST OF TABLES

LIST OF ACRONYMS

400ZR 400 Gb/s coherent optical interface standard.

ADC Analog-to-Digital Converter.

ASE amplified spontaneous emission.

BER Bit Error Ratio.

CD chromatic dispersion.

CFO carrier frequency offset.

CPR carrier phase recovery.

DAC Digital-to-Analog Converter.

DP dual polarization.

DP-16QAM dual-polarization 16-QAM.

DSP Digital Signal Processing.

DWDM dense wavelength division multiplexing.

EVM error vector magnitude.

FEC forward error correction.

FFT fast Fourier transform.

FIR finite impulse response.

FWM four-wave mixing.

ITU-T International Telecommunication Union – Telecommunication Standardization Sector.

MIMO multiple-input multiple-output.

MSA Multi-Source Agreement.

MZM Mach–Zehnder modulator.

NPN nonlinear phase noise.

OSNR optical signal-to-noise ratio.

PAM4 pulse amplitude modulation.

PDL polarization-dependent loss.

PMD polarization-mode dispersion.

PRBS pseudorandom bit sequence.

QAM quadrature amplitude modulation.

QPSK quadrature phase-shift keying.

ROADM Reconfigurable Optical Add-Drop Multiplexer.

RRC Root-Raised Cosine.

SBS stimulated Brillouin scattering.

SDN software-defined network.

SPM self-phase modulation.

SRS stimulated Raman scattering.

SSFM split-step Fourier method.

SSMF standard single-mode fiber.

WDM wavelength division multiplexing.

XPM cross-phase modulation.

XPolM cross-polarization modulation.

LIST OF SYMBOLS

f	Optical carrier frequency or baseband frequency
λ	Optical wavelength
$A_x,\ A_y$	Complex envelopes of the X and Y polarizations
$P_x,\ P_y$	Instantaneous power of the X and Y polarizations
P	Total instantaneous symbol power
$\Delta\phi$	Phase increment or nonlinear phase error of the symbol
$E_{\mathrm{TX}}, E_{\mathrm{RX}}$	Transmitted and received optical fields
α	Fiber attenuation
D	Chromatic dispersion parameter
L	Optical link length
A_{eff}	Effective mode area of the fiber
n_2	Nonlinear refractive index coefficient
$\Delta\nu$	Laser linewidth
γ	Nonlinear coefficient
$h(t)$	Impulse response of the receive filter
G_{EDFA}	Optical amplifier (EDFA) gain
NF	Noise figure of the EDFA
P_{ASE}	ASE noise power
T_s	Symbol period
EVM	Error Vector Magnitude
BER	Bit Error Ratio
SER	Symbol Error Ratio
ρ	Correlation coefficient between variables
M	QAM modulation order
SpS	Samples per symbol
f_0	Central frequency of the optical filter

CONTENTS

1 INTRODUCTION

1.1 DIGITAL COHERENT SYSTEMS

Coherent optical communication has reshaped modern networks by enabling transmission at extremely high data rates with superior spectral efficiency. These systems have become increasingly prevalent in short- and medium-reach applications, particularly within standardized interfaces such as 400ZR. Their operation relies on coherent detection combined with advanced DSP techniques, which compensate for key linear impairments including chromatic dispersion and polarization-mode dispersion.

Despite their sophistication, coherent transceivers remain fundamentally constrained by noise accumulation—especially ASE noise introduced by inline amplifiers—and by fiber nonlinearities such as SPM, XPM, and FWM. These effects introduce amplitude and phase distortions, degrade constellation quality, and reduce the available OSNR margin. Understanding how such impairments evolve and interact during propagation is essential for evaluating the performance limits of high-capacity coherent systems.

1.2 OBJECTIVES AND JUSTIFICATION

The main objective of this work is to characterize how nonlinear impairments affect dual-polarization coherent transmission operating under 400ZR-class conditions. To enable full control over the physical parameters of propagation and to access intermediate signal states not available in commercial tools, a complete numerical simulator was developed in Python using the Manakov equation and SSFM-based propagation.

The model is validated using BER curves only as a global performance reference, ensuring that the implemented propagation and DSP blocks remain consistent with industry-standard behavior. Once validated, the simulator is used to investigate nonlinear propagation at a finer scale, with emphasis on symbol-level effects such as phase distortions, intra- and inter-polarization interactions, and power-dependent transitions that remain hidden to traditional metrics.

This work is justified by the increasing relevance of understanding nonlinearities beyond aggregate metrics such as BER or EVM. Modern coherent interfaces—especially those based on the 400ZR specification—operate in conditions where deterministic nonlinear structures may exist even when global performance appears unaffected. A symbol-level analysis therefore provides insights that cannot be captured by conventional system-level evaluations, offering a deeper understanding of the physical limitations and operational boundaries of 400ZR links and supporting the development of future coherent technologies.

1.3 DOCUMENT STRUCTURE

This document is organized into six chapters and one appendix, as outlined below:

- **Chapter 2** introduces the 400ZR standard and its extensions, covering application context, system architecture, physical layer aspects, interoperability considerations, and advanced implementations such as 400ZR+.

- **Chapter 3** discusses the main fiber nonlinear effects relevant to 400ZR-like systems, including SPM, XPM, and FWM, as well as their impact on coherent receivers.

- **Chapter 4** presents the simulation setup and methodology, detailing the Python-based single- and multi-channel coherent models, the propagation framework, the implemented DSP, and the nonlinear interaction metrics used throughout this study.

- **Chapter 5** provides the results and nonlinear analysis, including intra-channel nonlinear behavior, residual nonlinear phase evolution, and inter-channel nonlinearities in wavelength division multiplexing (WDM) 400ZR transmission, particularly XPM and FWM interactions.

- **Chapter 6** concludes the study by summarizing the main findings, presenting the final conclusions, and outlining opportunities for future work.

- **Appendix A** describes in full detail the DSP algorithms used for coherent signal recovery, including chromatic dispersion compensation, polarization demultiplexing, frequency-offset estimation, and carrier-phase recovery.

2 400 ZR AND ITS UPGRADES

2.1 THE 400ZR STANDARD

In recent years, the exponential growth of data traffic between data centers and metro networks has driven the need for high-capacity, interoperable, and cost-effective optical solutions (CISCO, 2022). In this context, the 400ZR standard, defined by the OIF, has emerged as a robust solution for short- and medium-haul dense wavelength division multiplexing (DWDM) coherent transmissions, enabling line rates up to 400 Gbps per wavelength (OIF, 2020). Designed for point-to-point links of up to approximately 120 km, the 400ZR employs dual polarization (DP) 16 quadrature amplitude modulation (QAM) modulation and advanced DSP to mitigate impairments such as chromatic dispersion and polarization-related distortions as well as frequency offset and phase noise. Operating in the C-band, the system relies on standardized 100 GHz DWDM channel spacing as specified in the ITU-T G.694.1 by the International Telecommunication Union – Telecommunication Standardization Sector (ITU-T) recommendation (ITU-T, 2012).

A key innovation of the 400ZR lies in its interoperability between pluggable coherent transceivers, allowing modules from different vendors to operate jointly as long as they comply with a set of minimum physical requirements. These requirements include constraints on OSNR, polarization-dependent loss (PDL), and polarization-mode dispersion (PMD). The standard specifies both electrical and optical interfaces, as well as requirements for clocking, framing, and forward error correction (FEC), ensuring reliable performance in amplified and unamplified links (IEEE, 2017; CIENA, 2023). By enabling this interoperability in a pluggable form factor, the 400ZR has accelerated the deployment of coherent optics in metro-scale applications.

2.2 APPLICATION CONTEXT AND MOTIVATION

The growing demand for Data Center Interconects (DCI), fueled by cloud services, artificial intelligence workloads, and high-definition video traffic, has emphasized the need for optical links that combine high throughput, low latency, and seamless integration with existing architectures. Within this scenario, DCI has become a strategic segment that demands solutions with high traffic density and simplified operation. Traditional coherent technologies, originally designed for long-haul transmission, often present excessive cost and complexity when applied to shorter links. The 400ZR was conceived precisely to fill this gap by standardizing the use of pluggable coherent transceivers in point-to-point DWDM networks up to 120 km (FORUM, 2020; CISCO, 2022).

By relying on interoperable transceivers and avoiding the need for optical-electrical-optical regeneration or proprietary transponders, the 400ZR enables networks with lower cost per bit, higher optical port density, and direct integration into routers and switches. This makes it a strategic technology for metro and edge infrastructures, where cost and efficiency are decisive factors. The adoption of advanced concatenated FEC schemes provides additional robustness, ensuring reliable operation even in networks that may involve optical amplification or legacy passive elements (CISCO, 2022; CIENA, 2023).

2.3 SYSTEM ARCHITECTURE AND PHYSICAL LAYER ASPECTS

The 400ZR standard is based on a modular architecture that defines both the electrical host interface and the optical line interface. On the electrical side, the specification adopts the 400GAUI-8 interface, which consists of eight lanes of 56 Gbps pulse amplitude modulation (PAM4) signals, fully compatible with the 400GBASE-R protocol defined in IEEE 802.3bs (IEEE, 2017). These electrical streams are processed by a DSP that performs scrambling, interleaving, FEC, and mapping into the DP-16QAM modulation format. The optical interface follows the Black Link concept, whereby only the input and output parameters of the optical channel are standardized, regardless of the internal configuration of the network. This ensures that modules can be integrated seamlessly into heterogeneous infrastructures while still meeting interoperability requirements (FORUM, 2020; CISCO, 2023b).

The physical layer performance of the 400ZR is closely linked to its ability to tolerate various optical impairments. The use of DP-16QAM allows for four bits per symbol per polarization, achieving high spectral efficiency while keeping implementation complexity manageable. Transmission occurs in the C-band (approximately 1528–1567 nm), using 100 GHz fixed-grid DWDM channels in accordance with ITU-T recommendations (ITU-T, 2012). The system requires a minimum OSNR of about 26–30 dB for proper operation, while the maximum allowable PDL is specified as < 3 dB and PMD as < 10 ps. The standard also defines tolerances for chromatic dispersion up to 10,000 ps/nm, which are fully compensated through DSP, eliminating the need for passive dispersion compensators. Moreover, the 400ZR specifies two application codes: 0x01 for amplified links (with or without passive elements) and 0x02 for short direct-detection links below 10 km, typically without amplification (FORUM, 2020; CISCO, 2023a; CIENA, 2023).

2.4 USE CASES AND INTEROPERABILITY

The primary use case for the 400ZR is in DCI, where the pluggable modules can be inserted directly into switches or routers, eliminating the need for dedicated transponders and significantly reducing both energy consumption and rack space. This approach is strongly supported by industry players, including Cisco, which highlights the operational and cost benefits of coherent pluggables in DCI scenarios (CISCO, 2023a). In metro networks with point-to-point links, the 400ZR has gained traction due to its compatibility with existing optical infrastructures, leveraging legacy DWDM fixed-grid networks while also supporting emerging FlexGrid architectures for improved spectral efficiency. Furthermore, hyperscale providers and telecom operators have increasingly embraced the 400ZR within disaggregated network architectures, allowing for vendor flexibility and software-based control. By aligning with software-defined network (SDN) principles, the 400ZR fosters programmable, performance-centric optical networks.

Interoperability is a cornerstone of the standard. By defining precise physical, electrical, and optical parameters, the OIF implementation agreement ensures that modules from different vendors can operate jointly without compromising performance (FORUM, 2020). Compatibility with DWDM grids is guaranteed through the adoption of ITU-T G.694.1, supporting at least 48 channels with 100 GHz spacing, and extendable to 75 GHz or flexible-grid configurations when supported by the physical layer. Compliance methodologies include pseudorandom bit sequence (PRBS) testing, BER validation, error vector magnitude (EVM) analysis, and FEC performance verification. Through these requirements, the 400ZR achieves true multivendor interoperability, reducing operational costs and enabling large-scale deployment in open optical ecosystems, including operation in multi-channel WDM systems beyond the traditional four-channel configurations (CISCO, 2023b).

2.5 ADVANCED IMPLEMENTATIONS: 400ZR+

Although the 400ZR has been consolidated as an essential standard for short-reach coherent interconnections, its reach is inherently limited to about 120 km. In practical scenarios such as extended metro networks or regional backbones, there is a clear demand for longer reach and greater operational flexibility. To address these needs, the industry developed the 400ZR+, also known as OpenZR+, as a practical extension of the 400ZR philosophy. Unlike the OIF-standardized 400ZR, the 400ZR+ emerged from a Multi-Source Agreement (MSA) supported by vendors such as Infinera, Cisco (Acacia), Ciena, and Adtran, aiming to extend the applicability of coherent pluggables beyond pure DCI use cases (MSA, 2023; OPTICS, 2024).

The main advantage of the 400ZR+ lies in its extended reach, supporting distances up to 400–500 km by allowing operation with different modulation formats, including DP-16QAM, 8QAM, and quadrature phase-shift keying (QPSK). This modulation flexibility enables adaptive adjustment of the line rate, ranging from 100 to 400 Gb/s, depending on link conditions. In addition, the 400ZR+ is designed to operate in Reconfigurable Optical Add-Drop Multiplexer (ROADM)-enabled networks, greatly expanding its use cases into metro and regional infrastructures. These improvements, however, come at the cost of increased DSP complexity, more powerful FEC (e.g., OpenFEC), and higher power consumption, which may reduce port density compared to 400ZR solutions. Another important distinction is that, as a MSA-based specification rather than an OIF formal standard, interoperability may vary depending on vendor implementations (FORUM, 2024; FORUM, 2025; ADTRAN, 2025).

In summary, the 400ZR+ extends the reach and versatility of coherent pluggables, complementing the 400ZR in scenarios that demand greater transmission distances, operational flexibility, and compatibility with reconfigurable optical networks. By bridging the gap between short-reach DCI and regional networks, the 400ZR+ paves the way for more scalable and adaptive optical infrastructures while preserving the principles of openness and integration that defined the success of the 400ZR (MSA, 2023; OPTICS, 2024; ADTRAN, 2025; CISCO, 2022). A direct comparison between the two standards is presented in Table 1, highlighting their main similarities and differences.

Table 1 – Comparison between 400ZR and 400ZR+ standards

Feature	**400ZR**	**400ZR+ (OpenZR+)**
Standardization	OIF Implementation Agreement (OIF-400ZR-01.0)	Multi-Source Agreement (MSA)
Reach	Up to ∼120 km (point-to-point DCI)	Up to ∼400–500 km (metro/regional)
Modulation Formats	Fixed DP-16QAM	Flexible: DP-16QAM, 8QAM, QPSK
Line Rate	400 Gb/s fixed	Flexible: 100–400 Gb/s
Applications	Data Center Interconnects (DCI), short metro links	Extended metro, regional networks, ROADM-based infrastructures
FEC	Concatenated FEC (e.g., KP4 + hard-decision)	OpenFEC (OFEC), stronger codes for longer reach
Power Consumption	Lower (optimized for density and cost per bit)	Higher (due to more complex DSP and FEC)
Interoperability	Guaranteed by OIF standardization	Vendor-dependent (MSA, not formal OIF standard)

Source: Elaborated by the author.

3 NONLINEAR EFFECTS IN 400ZR-LIKE SYSTEMS

3.1 INTRODUCTION TO FIBER NONLINEARITIES

In optical fiber transmission, several nonlinear phenomena arise from the interaction between light and the medium. Stimulated scattering processes such as stimulated Brillouin scattering (SBS) and stimulated Raman scattering (SRS), as well as nonlinear refraction effects like the Pockels and Kerr effects, are usually considered (AGRAWAL, 2019). In the context of digital coherent systems such as 400ZR, SBS and SRS are not critical limitations: SBS primarily affects narrow-linewidth continuous-wave carriers, but in coherent systems such as 400ZR the optical carrier is strongly suppressed by high-baud-rate modulation, which spreads the spectrum and mitigates Brillouin gain. In contrast, SRS becomes significant only in very long-haul multi-channel links with high accumulated optical power, which is beyond the metro distances targeted by 400ZR (AGRAWAL, 2019; KEISER, 2021). The Pockels effect, although part of the same family of phase modulation phenomena, requires non-centrosymmetric materials and therefore does not occur in silica-based optical fibers. Consequently, the Kerr effect dominates nonlinear propagation in 400ZR-like links, leading to phase and amplitude distortions manifested as SPM, XPM, and FWM (AGRAWAL, 2019).

The Kerr effect describes the intensity dependence of the refractive index in optical fibers. Thus, the refractive index can be expressed as:

$$n = n_0 + n_2 I, \tag{1}$$

where n_0 is the linear refractive index, n_2 is the nonlinear index coefficient, and I is the optical intensity. This nonlinear contribution modifies the phase of the propagating field, giving rise to a range of effects such as SPM, XPM and FWM.

To quantify the impact of this effect on fiber propagation, it is common to define the nonlinear parameter γ, given by

$$\gamma = \frac{2\pi n_2}{\lambda A_{\text{eff}}}, \tag{2}$$

where λ is the operating wavelength and A_{eff} is the effective area of the fiber mode. The parameter γ represents the strength of the Kerr-induced phase shift per unit power and length, and thus plays a central role in evaluating nonlinear impairments in coherent optical systems. In the C-band, typical values of γ for standard single-mode fiber are around 1.2 W^{-1}km^{-1}, while fibers with reduced effective area can exhibit higher values, leading to stronger nonlinear distortions (AGRAWAL, 2019).

The impact of the Kerr effect on signal propagation in DP coherent systems is described by the coupled nonlinear Schrödinger equations, commonly referred to as the Manakov equations (AGRAWAL, 2019; POGGIOLINI, 2012; MECOZZI; ESSIAMBRE, 2012). These equations govern the evolution of the complex envelopes $A_x(t, z)$ and $A_y(t, z)$ of the optical field in the two orthogonal polarizations as the signal propagates along the fiber. They can be written as

$$\frac{\partial A_x(t,z)}{\partial z} - \frac{\alpha}{2}A_x(t,z) + \frac{j\beta_2}{2}\frac{\partial^2 A_x(t,z)}{\partial t^2} = j\frac{8}{9}\gamma\left(|A_x(t,z)|^2 + |A_y(t,z)|^2\right)A_x(t,z), \tag{3}$$

$$\frac{\partial A_y(t,z)}{\partial z} - \frac{\alpha}{2}A_y(t,z) + \frac{j\beta_2}{2}\frac{\partial^2 A_y(t,z)}{\partial t^2} = j\frac{8}{9}\gamma\left(|A_x(t,z)|^2 + |A_y(t,z)|^2\right)A_y(t,z), \tag{4}$$

where α denotes the fiber attenuation coefficient, β_2 the group-velocity dispersion parameter, and γ the nonlinear coefficient defined previously. The factor $8/9$ accounts for the statistical averaging over fast polarization variations, which makes the nonlinear interaction effectively isotropic between the two polarizations. These equations clearly show how chromatic dispersion, fiber loss, and Kerr nonlinearity jointly affect the transmitted signal in 400ZR-like systems (AGRAWAL, 2019).

While the Manakov equations describe the combined action of fiber attenuation, chromatic dispersion, and Kerr nonlinearity, it is common in the literature to isolate the nonlinear terms in order to explain SPM, XPM, and FWM. This pedagogical simplification, often adopted in standard references (AGRAWAL, 2019; KEISER, 2021), highlights the fundamental role of the Kerr-induced phase shift before reintroducing dispersion and loss effects in complete models, since in practical coherent systems such as 400ZR, these effects always act simultaneously, with dispersion and attenuation shaping the strength and manifestation of the nonlinear distortions.

3.2 SELF-PHASE MODULATION (SPM)

The simplest manifestation of the Kerr effect in optical fibers is SPM. In the general case, the nonlinear Schrödinger equation for the i-th channel or polarization can be written in (5).

$$\frac{\partial A_i}{\partial z} = j\gamma\left(|A_i|^2 + \sum_{j\neq i}|A_j|^2\right)A_i. \tag{5}$$

In (5), when only a single channel is present, the summation vanishes and the equation reduces to the pure SPM contribution:

$$\frac{\partial A_i}{\partial z} = j\gamma|A_i|^2 A_i. \tag{6}$$

The nonlinear phase shift accumulated during propagation is proportional to the optical power:

$$\phi_{\mathrm{NL}}(z) = \gamma P(z) L, \tag{7}$$

where $P(z) = |A_i(z)|^2$ is the optical power and L is the length of the fiber.

SPM introduces a time-varying phase shift within each symbol, leading to spectral broadening, particularly in the presence of chromatic dispersion. In coherent systems such as 400ZR, DSP partially mitigates its impact, but SPM still represents a fundamental source of nonlinear distortion (AGRAWAL, 2019).

3.3 CROSS-PHASE MODULATION (XPM)

Another important manifestation of the Kerr effect is XPM, in which the intensity of one wave induces a nonlinear phase shift in another. In WDM systems, the effect can be expressed as:

$$\frac{\partial A_i}{\partial z} = j\gamma \left(\sum_{j \neq i} |A_j|^2 \right) A_i, \tag{8}$$

where the summation accounts for the nonlinear coupling among channels j and the channel of interest i. This equation highlights that the power fluctuations of neighboring WDM channels contribute to the nonlinear phase of the analyzed channel. In the particular case of two interacting channels, the expression reduces to the well-known form in which the cross-phase modulation term is weighted by a factor of 2 relative to SPM (AGRAWAL, 2019).

In DP transmission, a similar mechanism occurs between orthogonal polarizations of the same channel. In this case, the Manakov equations describe the phenomenon as

$$\frac{\partial A_x}{\partial z} = j\gamma \left(|A_x|^2 + |A_y|^2 \right) A_x, \tag{9}$$

$$\frac{\partial A_y}{\partial z} = j\gamma \left(|A_y|^2 + |A_x|^2 \right) A_y, \tag{10}$$

where the cross terms $|A_y|^2 A_x$ and $|A_x|^2 A_y$ represent the influence of one polarization on the phase of the other. The statistical averaging of the state of polarization along the fiber ultimately leads to an effective weighting factor of $8/9$ for the nonlinear interaction, as already noted in the Manakov model.

Finally, at very high symbol rates such as those employed in 400ZR (56 Gbaud with DP-16QAM), chromatic dispersion induces temporal overlap between adjacent symbols within the same channel. As a result, the nonlinear phase of each symbol depends not only on its own power but also on that of neighboring symbols. This intra-channel coupling, often referred to as *intra-channel XPM* or cross-symbol interference, is usually encompassed within analytical models of nonlinear interference rather than treated as an isolated effect (AGRAWAL, 2019; KEISER, 2021).

3.4 FOUR-WAVE MIXING (FWM)

Another nonlinear mechanism arising from the Kerr effect is FWM. In its general form, FWM originates from the nonlinear interaction among multiple frequency components of the optical field. The contribution of FWM to the evolution of the i-th channel can be expressed as

$$\left. \frac{\partial A_i}{\partial z} \right|_{\text{FWM}} = j\gamma \sum_{j,k,l} A_j A_k A_l^* e^{j\Delta\beta z}, \tag{11}$$

where the exponential term includes the phase mismatch

$$\Delta\beta = \beta(\omega_j) + \beta(\omega_k) - \beta(\omega_l) - \beta(\omega_i). \tag{12}$$

For example, in the particular case where three distinct waves at frequencies ω_1, ω_2, and ω_3 interact, a new wave is generated at

$$\omega_4 = \omega_1 + \omega_2 - \omega_3. \tag{13}$$

This expression highlights the frequency conversion nature of FWM. The efficiency of the process depends strongly on the phase-matching condition $\Delta\beta \approx 0$, which is determined by the fiber dispersion. In low-dispersion transmission regimes, phase matching is favored, and FWM becomes particularly detrimental, limiting the usable channel spacing and launch power.

In WDM systems, the interaction among channels leads to the generation of new spectral components that may overlap with existing signals, creating inter-symbol interference. In polarization-multiplexed systems, the Manakov equations predict that nonlinear interaction terms include contributions from both polarizations. Consequently, FWM products can also involve energy transfer between orthogonal polarizations, although random polarization variations tend to average out this effect over long distances.

Beyond inter-channel interactions, in high-baudrate coherent systems such as 400ZR, FWM can also occur between different symbols within the same channel, a phenomenon known as *intra-channel four-wave mixing* (IFWM). Due to chromatic dispersion, optical pulses spread in time, leading to temporal overlap between adjacent and non-adjacent symbols. This overlap allows three distinct symbols to mix and generate spurious components that fall within the same spectral band. Unlike inter-channel FWM, which produces well-defined new frequencies, IFWM manifests as a distortion term that contributes to the overall nonlinear interference accumulated along the fiber (AGRAWAL, 2019; POGGIOLINI, 2012).

3.5 SYSTEM IMPAIRMENTS IN DIGITAL COHERENT RECEIVERS

In addition to nonlinear distortions arising from the Kerr effect, digital coherent transceivers are affected by a variety of physical and electronic impairments that must be mitigated through advanced signal processing techniques. These impairments originate both in the optical domain—during signal propagation through the fiber—and in the electrical domain—within the transmitter and receiver circuitry (SAVORY, 2008; SAVORY, 2012; ZHAO; LIU; XU, 2019; NETO; ALDAYA et al., 2020).

From the optical perspective, chromatic dispersion (CD) and PMD cause temporal and polarization-dependent spreading of the transmitted symbols. These linear effects are deterministic and can be efficiently compensated by digital filters implemented in the receiver, which invert the transfer function of the optical channel. On the other hand, nonlinear phase noise (NPN), XPM and FWM introduce stochastic-like distortions that are power-dependent and not fully invertible, requiring more sophisticated nonlinear equalization schemes.

In the electronic domain, impairments such as in-phase/quadrature (I/Q) imbalance, Mach–Zehnder modulator (MZM) nonlinearity, and Digital-to-Analog Converter (DAC)/Analog-to-Digital Converter (ADC) distortion degrade the orthogonality of the transmitted signals and distort the constellation. Additionally, frequency offset and phase noise between the transmitter and local oscillator lasers lead to constellation rotation and broadening, which must be dynamically tracked by algorithms.

Table-based architectures of DSP modules in 400ZR-class transceivers typically include:

1. **Orthogonalization and normalization**, to correct I/Q imbalance and polarization misalignment;
2. **Chromatic dispersion equalization**, often implemented in the frequency domain;
3. **Adaptive multiple-input multiple-output (MIMO) equalization**, to compensate PMD and polarization crosstalk;
4. **Timing and frequency synchronization**, including clock recovery and carrier frequency offset (CFO) estimation;
5. **Carrier phase estimation**, to mitigate laser phase noise;
6. **Optional** such as digital backpropagation (DBP) or Volterra-based equalizers.

These DSP modules collectively restore the orthogonality and temporal alignment of the received signal, allowing coherent detection to approach the theoretical Shannon limit. In practice, the efficiency of compensation depends on the dynamic nature of the impairments: while dispersion and I/Q imbalance are quasi-static, frequency and phase noise vary rapidly and require adaptive, real-time tracking (SAVORY, 2008; ZHAO; LIU; XU, 2019). More detailed description can be found in Appendix A.

4 SIMULATION SETUP AND METHODOLOGY

The numerical investigation presented in this work is based on two complementary strategies: (i) a reference coherent transmission model implemented in *VPItransmissionMaker*, used as a benchmark for physical accuracy, and (ii) a fully transparent and reproducible Python-based simulator developed specifically for this study. By comparing the results obtained from both environments, the proposed Python model can be rigorously validated, while also providing controlled conditions for analyzing the deterministic nonlinear interactions that arise in dual-polarization 16-QAM transmission under 400ZR-class operating parameters.

The VPI implementation serves as a physically accurate benchmark for the optical front-end, fiber propagation, and coherent reception. However, its multi-channel WDM configuration exhibits residual artifacts that limit its use for detailed nonlinear analysis. This motivated the construction of an independent Python framework in which all processes—signal generation, propagation, noise loading, and DSP—are explicitly accessible and can be selectively enabled or disabled. By reproducing the same transmission parameters in both environments, it becomes possible to verify the consistency of the Python model and to isolate nonlinear effects without tool-induced distortions.

All stages of DSP required for coherent reception—such as CD compensation, polarization demultiplexing, carrier-frequency offset estimation, and carrier-phase recovery—are implemented identically in both simulation platforms. A complete description of these DSP algorithms is provided in Appendix A, and they are omitted here to maintain the focus on the physical modeling and nonlinear analysis that constitute the core of this chapter.

With these elements established, the following sections present the methodology used to construct and validate the Python-based coherent model. The discussion begins with an overview of the VPI simulations used as a reference and then details the Python implementation, its single-channel validation, and its extension to multi-channel WDM propagation.

4.1 MOTIVATION FOR A PYTHON-BASED NUMERICAL MODEL

Although commercial simulation platforms such as *VPItransmissionMaker* provide accurate modeling of optical components, fiber propagation, and coherent reception, their closed architecture limits access to internal quantities essential for nonlinear analysis. Symbol-level phase evolution, instantaneous polarization coupling, and nonlinear perturbations cannot be directly extracted from block-diagram environments.

In addition, preliminary WDM simulations performed in VPI revealed an unexpected behavior: the outer channels displayed higher BER at low launch powers than the inner channels, despite all wavelengths experiencing identical attenuation, dispersion, and OSNR. Since this imbalance has no physical justification in standard single-mode fiber (SSMF) propagation, it indicates a tool-induced artifact rather than a fiber-induced effect. These observations motivated the development of a fully independent Python model that:

- Mirrors the physical parameters of the VPI reference model;
- Enables full control over symbol generation, propagation, and DSP;
- Allows direct access to the received envelopes for nonlinear analysis.

An important modeling choice is the exclusion of PMD, whose stochastic nature would obscure deterministic nonlinear interactions and require Monte Carlo averaging. Restricting the model to deterministic physical effects ensures reproducibility and facilitates quantitative analysis.

The resulting numerical framework provides a clean, transparent, and physically accurate environment suitable for investigating both intra-channel and inter-channel nonlinear interactions.

4.2 PYTHON-BASED SINGLE-CHANNEL COHERENT MODEL

The Python framework reproduces all stages of a dual-polarization 16-QAM coherent transceiver, including transmitter modeling, fiber propagation, and receiver-side DSP. The single-channel implementation forms the basis for validating the propagation model and DSP chain before extending the analysis to WDM operation.

4.2.1 Transmitter Model

The transmitter generates a sequence of Gray-mapped 16-QAM symbols. All physical and DSP parameters match those specified in Table 2, ensuring consistency with the reference VPI model.

Pulse shaping is implemented using a Root-Raised Cosine (RRC) filter within the DAC_Nyquist block. The X and Y polarizations are modulated independently using a MZM. A short synchronization sequence is appended to each polarization to enable frame alignment after propagation.

The resulting complex optical fields $A_x[n]$ and $A_y[n]$ serve as input to the fiber model.

4.2.2 Fiber Propagation Model

Propagation through SSMF is implemented using the split-step Fourier method (SSFM) (AGRAWAL, 2019). Each propagation step incorporates attenuation, chromatic dispersion, and Kerr nonlinearity, ensuring consistency with the physical behavior of standard single-mode fiber.

Attenuation.

Fiber loss is modeled through an exponential decay applied to both polarization components:

$$A_x \leftarrow A_x\, e^{-\alpha\,\Delta L}, \qquad A_y \leftarrow A_y\, e^{-\alpha\,\Delta L}, \tag{14}$$

where α is the power attenuation coefficient (in 1/km) and ΔL is the SSFM step size. This operator accounts for deterministic signal depletion along the fiber span.

Table 2 – Transmitter and system parameters used in the numerical model.

Parameter	Value
Modulation format	DP-16QAM
Symbol rate	56 GBd
Samples per symbol ()	8
RRC roll-off factor	0.1
Laser linewidth	100 kHz
Launch power per channel	0–12 dBm (sweep)
WDM spacing	75 GHz
Number of channels	1–4 (depending on experiment)
Fiber type	SSMF
Chromatic dispersion (D)	16 ps/nm/km
Nonlinearity coefficient (γ)	1.3 $\mathrm{W}^{-1}\mathrm{km}^{-1}$
Attenuation (α)	0.2 dB/km
Span length	80–120 km
EDFA noise figure	5 dB

Source: Elaborated by the author.

Chromatic dispersion.

The CD operator is implemented in the frequency domain and given by:

$$H_{\mathrm{CD}}(\omega) = \exp\left(-j\,\frac{D\,\lambda^2}{4\pi c}\,L\,\omega^2\right), \tag{15}$$

which introduces group-velocity dispersion–induced pulse broadening over the propagation length L.

Kerr nonlinearity.

The nonlinear phase rotation is applied independently to each polarization through:

$$A_x \leftarrow A_x\,\exp\big(j\gamma\,\Delta L\,\left(|A_x|^2 + |A_y|^2\right)\big), \qquad A_y \leftarrow A_y\,\exp\big(j\gamma\,\Delta L\,\left(|A_x|^2 + |A_y|^2\right)\big), \tag{16}$$

modeling both intrapolarization SPM and cross-polarization nonlinear mixing arising from the intensity dependence of the refractive index.

Excluded effect: PMD.

PMD is deliberately excluded from the model to maintain deterministic propagation and isolate nonlinear behavior without introducing stochastic polarization fluctuations.

4.2.3 Receiver and DSP

After fotodetection detection and ADC, the following DSP sequence is applied:

- CD inversion using Eq. (15);

- Frame and timing alignment via correlation with the preamble;
- CFO estimation via brute-force search;
- Amplitude normalization to match ideal 16-QAM symbol energy;
- Blind-phase-search carrier phase recovery (CPR) and
- Symbol decisions and Bit Error Ratio (BER) computation.

Once all linear impairments are mitigated, the received envelopes become suitable for nonlinear interaction analysis.

4.3 VALIDATION OF THE PYTHON COHERENT MODEL AGAINST THE VPI REFERENCE

To verify the physical consistency of the Python framework, a reduced reference model was implemented in *VPItransmissionMaker*. The transmitter and receiver architectures are shown in Figs. 1–3, while the physical parameters used in VPI match those listed in Table 2.

Figure 1 – Transmitter section of the VPI-based 400ZR reference model.

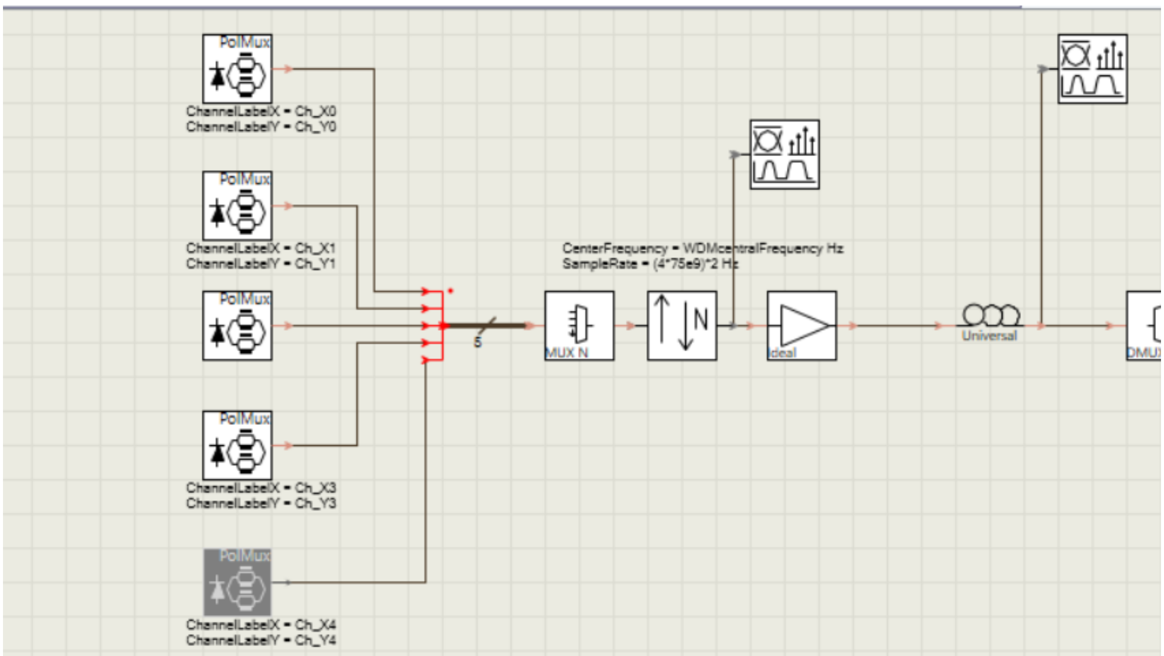

Source: Elaborated by the author.

Figure 2 – Receiver section of the VPI-based coherent model.

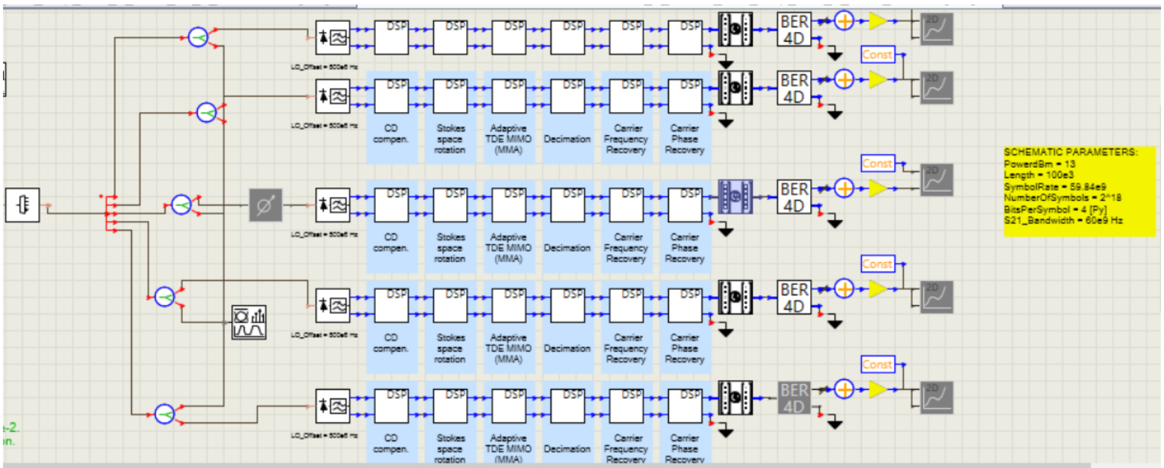

Source: Elaborated by the author.

Figure 3 – DSP chain used in the VPI reference simulation.

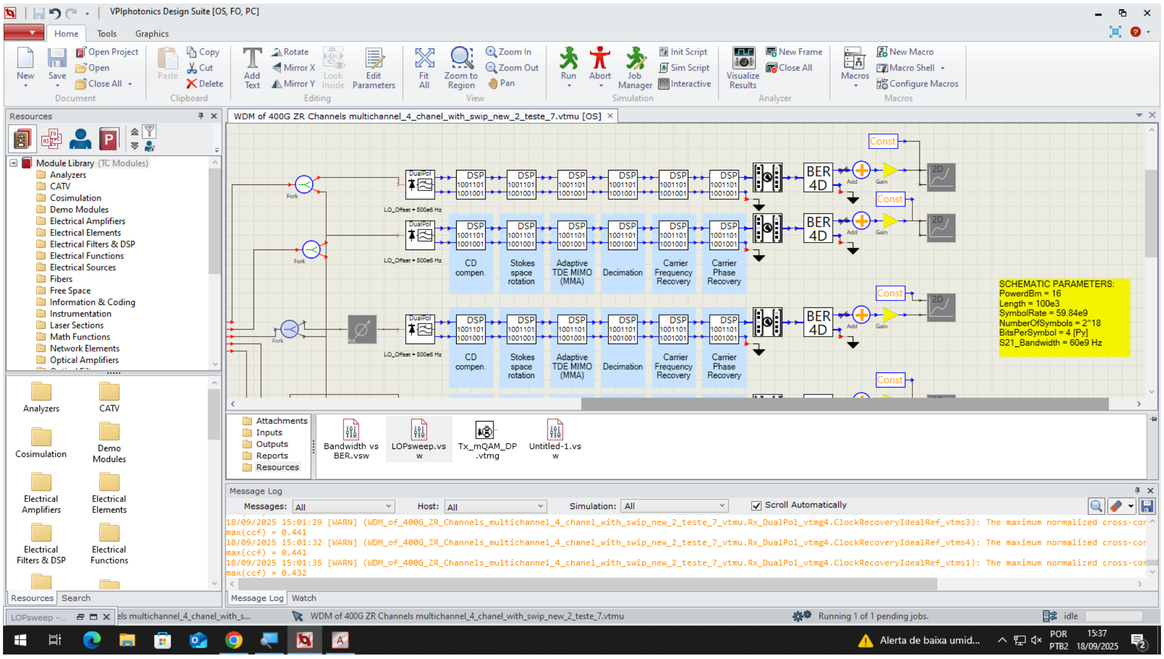

Source: Elaborated by the author.

Single-channel validation

A single-channel 80 km link was simulated using identical parameters in both tools. As shown in Fig. 4, the Python and VPI curves exhibit excellent agreement. Both models display OSNR-limited behavior at low powers and nonlinear penalties at high powers.

Figure 4 – BER comparison between Python and VPI for the 80 km single-channel link.

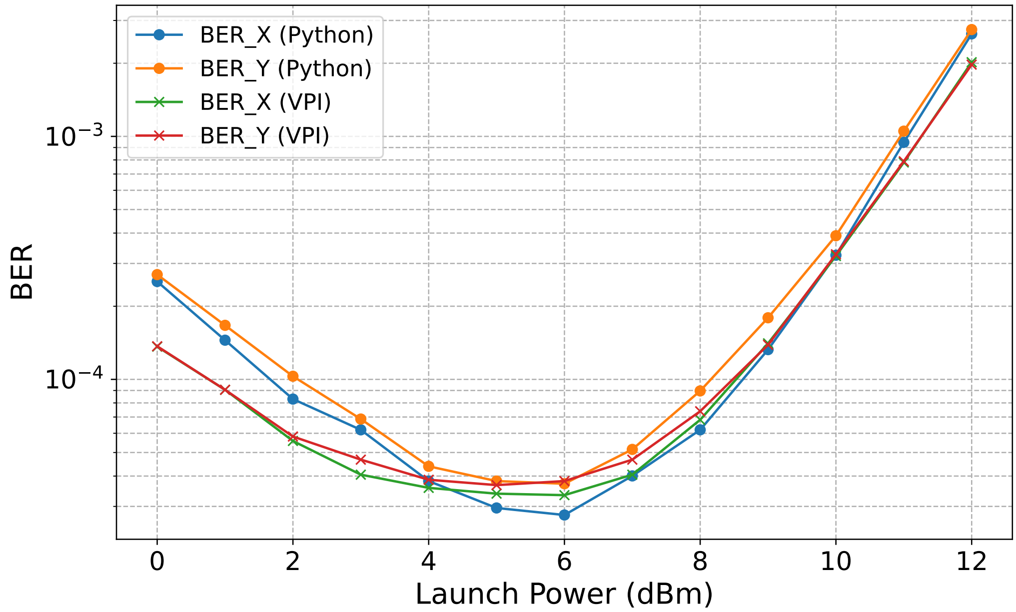

Source: Elaborated by the author.

Limitations of the VPI WDM reference

When the VPI model was extended to four WDM channels, an unexpected imbalance was observed: outer channels presented higher BER at low powers than inner channels, despite identical propagation conditions. This tool-induced artifact is shown in Fig. 5.

Figure 5 – BER curves for the four WDM channels in the VPI simulation at 80 km.

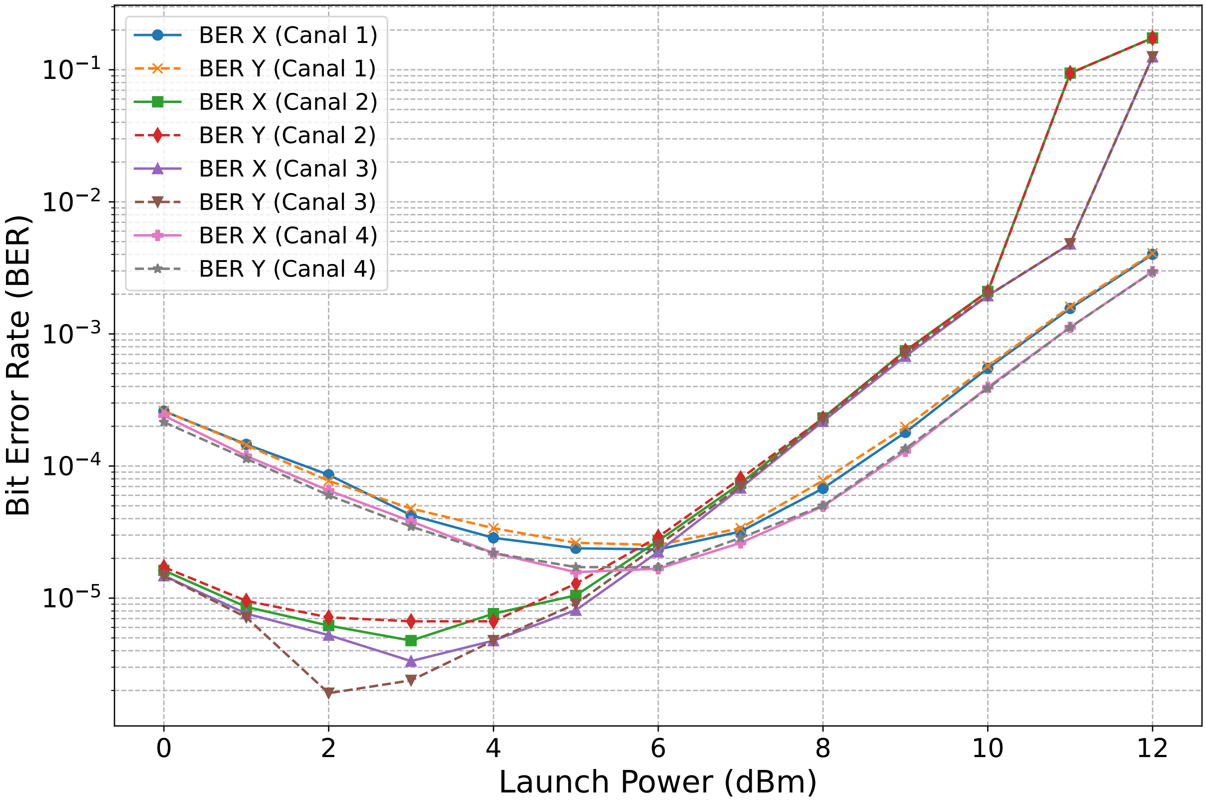

Source: Elaborated by the author.

Because this imbalance contradicts the expected symmetry of WDM propagation in SSMF, the Python model was adopted as the primary tool for nonlinear analysis.

Extended validation across multiple distances

The Python model was used to simulate 80, 100, and 120 km links. The BER curves in Fig. 6 follow the expected behavior: increased ASE accumulation at low powers and convergence at high powers due to nonlinear saturation.

Figure 6 – BER versus launch power for 80, 100, and 120 km links simulated in Python.

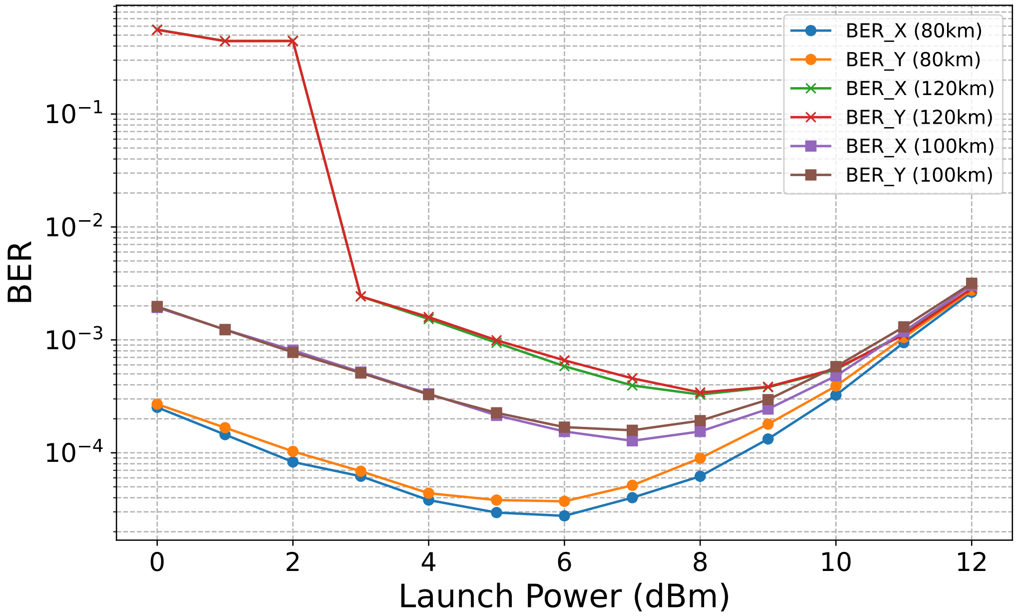

Source: Elaborated by the author.

These validation results confirm that the Python implementation is physically accurate and numerically consistent, providing a reliable foundation for the nonlinear analysis presented in Chapter 6.

4.4 NONLINEAR INTERACTION METRICS FOR SINGLE-CHANNEL ANALYSIS

4.4.1 SPM and XPolM Metrics

To quantify Kerr-induced nonlinearities, correlation-based metrics are computed from the received envelopes. Instantaneous power and nonlinear phase increments are defined as:

$$P_{x,y}[n] = |A_{x,y}[n]|^2, \qquad \Delta\phi_{x,y}[n] = \arg(A_{x,y}[n]) - \arg(A_{x,y}[n-1]).$$

The XPolM matrix measuring amplitude–phase coupling is:

$$\mathbf{C} = \begin{bmatrix} \mathrm{corr}(P_x,\, \Delta\phi_x) & \mathrm{corr}(P_x,\, \Delta\phi_y) \\ \mathrm{corr}(P_y,\, \Delta\phi_x) & \mathrm{corr}(P_y,\, \Delta\phi_y) \end{bmatrix}. \tag{17}$$

Diagonal terms represent co-polarization SPM, while off-diagonal terms quantify cross-polarization SPM. These coefficients reveal whether any deterministic Kerr-induced distortion remains after complete DSP compensation.

4.4.2 Residual Nonlinear Phase Analysis via Power–Phase Scatter

In addition to the correlation-based XPolM metric, a complementary diagnostic tool is adopted to visualize residual Kerr-induced distortions at the symbol level. This method evaluates the nonlinear phase deviation as a function of the instantaneous received power, providing a more detailed view of the onset of nonlinear propagation effects.

The residual phase error is defined as:

$$\Delta\phi[n] = \arg(A[n]) - \arg(\hat{A}[n]),$$

where $\hat{A}[n]$ is the nearest ideal constellation symbol obtained through minimum-distance decision. The instantaneous symbol power is computed as

$$P[n] = |A[n]|^2,$$

or per polarization when required.

Plotting $\Delta\phi[n]$ as a function of $P[n]$ yields the *power–phase scatter diagram*, which reveals how nonlinear phase distortions grow with symbol power. To emphasize the region in which nonlinear effects are most pronounced, a power threshold is introduced based on the 90th percentile of the power distribution:

$$P_{\mathrm{th}} = \mathrm{percentile}_{90}(P[n]).$$

Symbols above this threshold typically exhibit the strongest Kerr-induced rotations. In contrast to the XPolM correlation matrix, which provides a single global metric, the power–phase scatter enables direct visualization of the symbol-wise structure of nonlinear distortions. This makes the method especially useful for identifying subtle nonlinear behaviors that may remain hidden when considering only aggregated performance metrics such as BER or EVM.

4.5 PYTHON-BASED MULTI-CHANNEL COHERENT MODEL

With the single-channel validation established, the model was extended to a four-channel WDM configuration to analyze inter-channel nonlinear interactions under realistic 400ZR conditions. Unlike the VPI environment, the Python implementation enforces strict channel symmetry, eliminating tool-induced distortions.

4.5.1 WDM Propagation and DSP Implementation

Four dual-polarization 16-QAM (DP-16QAM) channels spaced by 75 GHz are independently modulated, pulse-shaped, and combined into a composite WDM signal. Each wavelength is launched with identical power.

Propagation uses the same dispersive–nonlinear operator described earlier. The receiver performs ideal optical filtering followed by the same DSP chain applied in the single-channel case. Because all channels undergo identical propagation and processing, the model provides a clean platform for nonlinear interaction analysis.

4.5.2 Cross-Phase Modulation (XPM) Metrics

For each ordered pair of channels (m, k), the XPM strength is defined as:

$$c_{k \leftarrow m} = \max_{\tau} \operatorname{corr}\big(P_m[n],\, \Delta\phi_k[n+\tau]\big).$$

The maximizing lag:

$$\tau^{\star} = \arg\max_{\tau} \operatorname{corr}\big(P_m[n],\, \Delta\phi_k[n+\tau]\big)$$

quantifies dispersion-induced walk-off.

4.5.3 Four-Wave Mixing (FWM) Metrics

Four-wave mixing (FWM) tones in a WDM system satisfy the frequency relation

$$f_{\text{FWM}} = f_i + f_j - f_k.$$

For a given victim channel v, the third participating channel k is implicitly defined by the FWM condition

$$f_i + f_j - f_k = f_v,$$

assuming a uniformly spaced WDM frequency grid.

For each valid non-degenerate channel quadruplet (i, j, k, v), the corresponding FWM field contribution is modeled as

$$S_{i,j,k}(n) = A_i(n)\, A_j(n)\, A_k^{*}(n),$$

where $A_m(n)$ denotes the complex baseband field of channel m.

The interaction strength associated with FWM impacting the victim channel v is quantified through a normalized correlation metric,

$$\rho_{v,i,j} = \operatorname{corr}\big(A_v(n), S_{i,j,k}(n)\big),$$

with k determined by the FWM frequency relation. Only non-degenerate interactions, for which i, j, k, and v are all distinct, are considered.

For each launch power, the resulting coefficients are assembled into 4×4 correlation matrices for each victim channel, forming the basis of the inter-channel FWM analysis presented in Chapter 5.

5 RESULTS AND NONLINEAR ANALYSIS

This chapter presents the results obtained from the numerical coherent model described in Chapter 4. The analysis is divided into two main parts. Section 5.1 investigates the nonlinear behavior of a single DP-16QAM channel and characterizes the residual Kerr-induced distortions that remain after the complete DSP chain. Section 5.2 extends the investigation to the four–channel WDM scenario, focusing on inter–channel nonlinearities—particularly XPM and FWM. Together, these results establish the relative strength and practical relevance of intra- and inter-channel nonlinear distortions under realistic 400ZR transmission conditions.

5.1 NONLINEAR PHENOMENA IN SINGLE-CHANNEL 400ZR TRANSMISSION

The single-channel analysis quantifies the influence of Kerr nonlinearities in a 400 Gb/s DP-16QAM coherent link over 100 km of SSMF, using launch powers of 0, 4, 8, and 12 dBm. As discussed in Chapter 5, traditional performance metrics such as BER and OSNR describe global signal degradation but do not reveal the microscopic structure of nonlinear amplitude–phase coupling. For this purpose, the analysis employs the nonlinear metrics defined in Section 4.4, including the cross-polarization modulation (XPolM) matrix and the power–phase scatter representation.

The chosen span length (100 km) provides a balanced regime where nonlinear effects become noticeable without excessive walk-off, ASE accumulation, or PMD randomization, making it representative of practical 400ZR deployments (AGRAWAL, 2019; MECOZZI; ESSIAMBRE, 2012; DAR et al., 2014).

5.1.1 XPolM-Based Quantification of Intra-Channel Nonlinearities

Figure 7 presents the XPolM matrices obtained after chromatic-dispersion compensation, 2×2 MIMO equalization, carrier-frequency offset removal, and carrier-phase recovery. Each matrix expresses the correlation between instantaneous power and nonlinear phase increments within and across the two polarizations, as defined in Section 4.4.1.

Figure 7 – XPolM correlation matrices computed for the single-channel 100 km 400ZR transmission at 0, 4, 8, and 12 dBm. The results confirm extremely low cross-polarization nonlinear coupling across all launch powers.

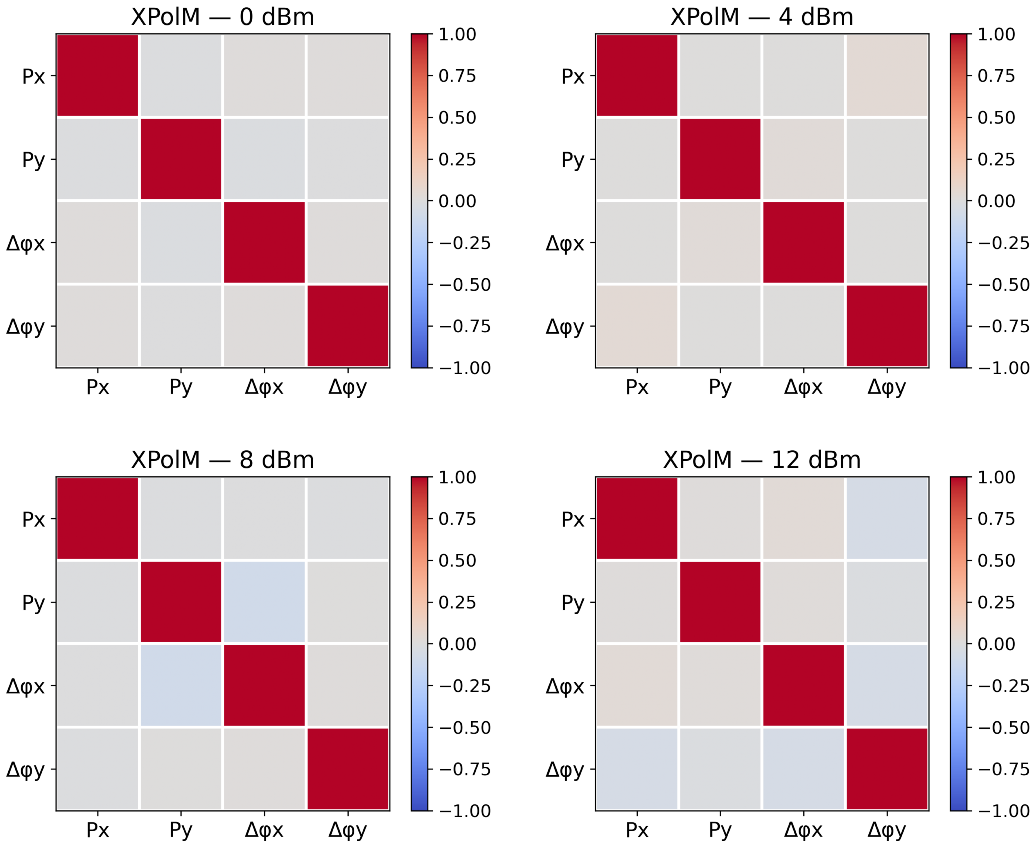

Source: Elaborated by the author.

Three distinct regimes emerge:

- **Low-power regime (0 dBm).** All entries are essentially zero, indicating fully linear behavior.
- **Moderate powers (4–8 dBm).** Diagonal coefficients (intrapolarization SPM) grow mildly, while cross-polarization terms remain negligible.
- **High-power regime (12 dBm).** SPM becomes more pronounced, but XPolM remains near zero, confirming polarization orthogonality is preserved.

These results match the theoretical expectation that dispersion and Manakov averaging suppress deterministic cross-polarization coupling in dual-polarization coherent systems (MECOZZI; ESSIAMBRE, 2012).

5.1.2 Residual Nonlinear Phase Behavior via Power–Phase Scatter Analysis

To complement the XPolM correlation analysis, the residual phase behavior was evaluated by applying the power–phase scatter method introduced in Section 4.4. This visualization highlights how nonlinear phase distortions emerge as the launch power increases and reveals whether such distortions follow a structured, deterministic pattern or remain noise-like after DSP compensation.

Figures 8, 9, and 10 present the scatter diagrams for 8, 11, and 12 dBm, respectively. In each case, the residual phase deviation is plotted against the instantaneous symbol power, with a vertical marker at the 90th percentile of the power distribution to emphasize the region where Kerr-induced effects are most pronounced.

Figure 8 – Power–phase scatter for 100 km single-channel transmission at 8 dBm. The distribution remains noise-like, indicating negligible nonlinear distortion.

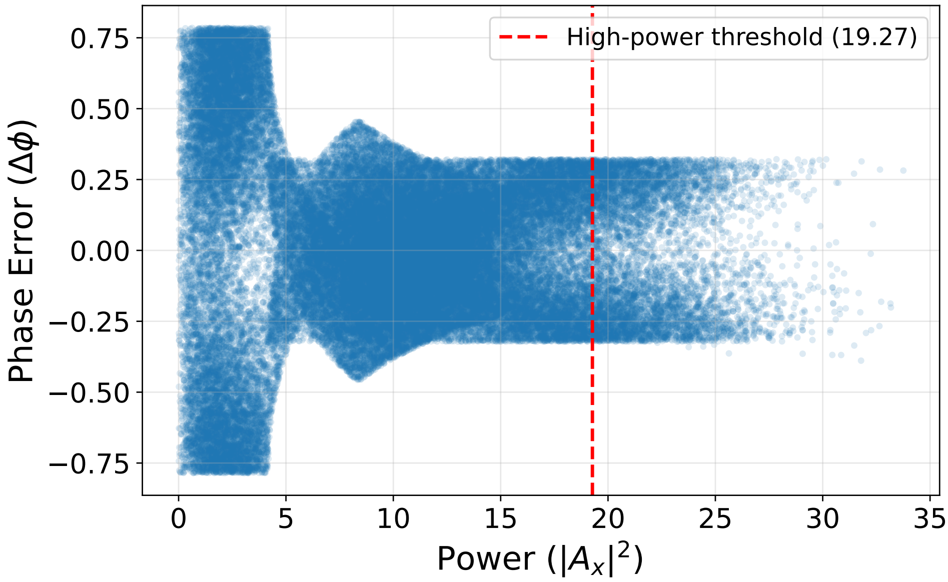

Source: Elaborated by the author.

Figure 9 – Power–phase scatter at 11 dBm. A structured, tilted pattern emerges above the 90th-percentile threshold, indicating the onset of Kerr-induced phase rotation.

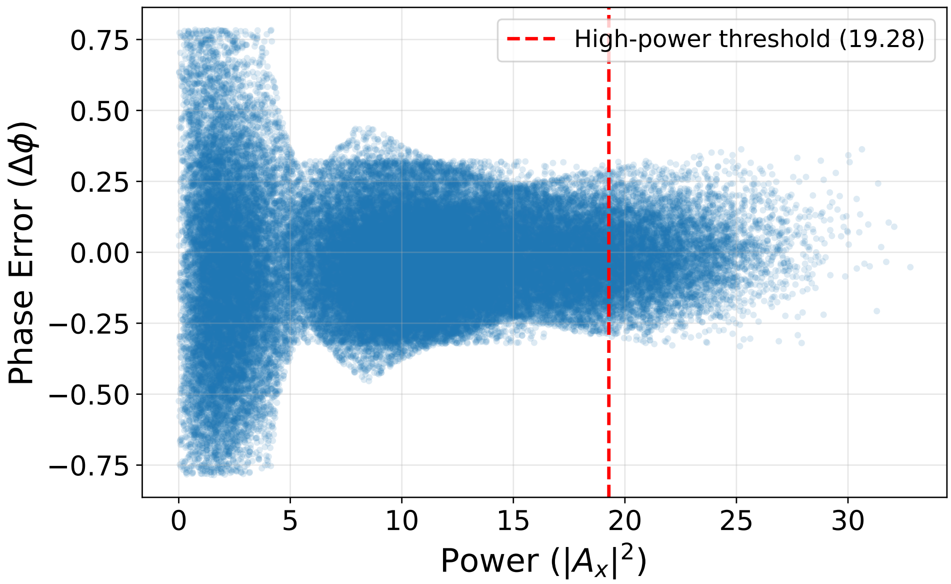

Source: Elaborated by the author.

Figure 10 – Power–phase scatter at 12 dBm. Strongly skewed phase behavior appears for high-power symbols, confirming the presence of nonlinear phase rotation.

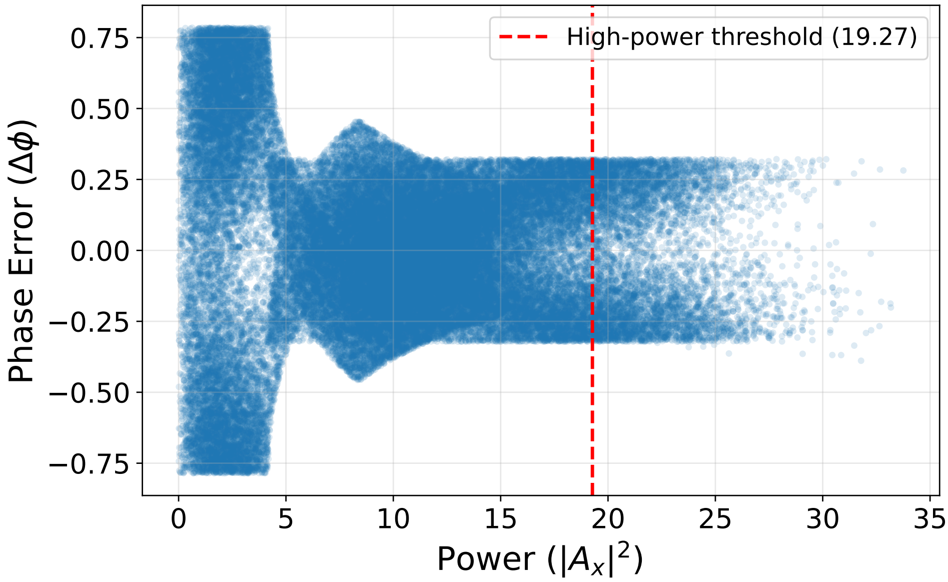

Source: Elaborated by the author.

The results reveal three distinct operating regions:

- At **8 dBm**, the phase–power cloud is fully symmetric and noise-like, indicating negligible nonlinear distortion.
- At **11 dBm**, a consistent tilted structure emerges for high-power symbols, marking the beginning of deterministic Kerr-induced phase rotation.
- At **12 dBm**, nonlinear behavior becomes clearly visible, with a strong asymmetric signature characteristic of SPM-dominated propagation.

These results confirm the existence of an intermediate region (10–11 dBm) in which nonlinear effects first become detectable at the symbol level, even though traditional global metrics such as BER or XPolM still indicate near-linear operation. This transitional regime provides important insight into the onset of nonlinear penalties and motivates further investigation in future work.

5.2 NONLINEAR EFFECTS IN MULTICHANNEL 400ZR TRANSMISSION

This section extends the analysis to the four–channel WDM configuration with 75 GHz spacing. In this scenario, nonlinear interactions arise not only within each wavelength but also between them. Two mechanisms are of primary importance: cross–phase modulation (XPM), which represents the dominant inter–channel effect, and FWM, a weaker parametric interaction generated by triplets of channels. The metrics adopted follow directly from the definitions introduced in Section 4.5.

Before presenting the WDM correlation results, it is important to clarify the meaning of the peak–lag correlation matrices used throughout this section. For each pair of channels, the correlation metric is evaluated not only at zero temporal alignment, but across a small window of symbol offsets that captures the relative delay between the interfering and victim waveforms. This offset, referred to as the *lag*, corresponds to the number of symbol intervals by which one sequence is shifted relative to the other during the computation of the correlation.

In physical terms, the lag reflects the fact that nonlinear interactions in multi–channel WDM systems are not instantaneous. Because each wavelength propagates with a slightly different group velocity, the power fluctuations of an interfering channel do not overlap perfectly with the symbols of the victim channel. As a result, the strongest nonlinear interaction frequently occurs at a small positive or negative temporal offset. By sweeping the lag across this window and selecting the maximum absolute correlation value, the peak–lag metric identifies the point of strongest inter–channel coupling.

This interpretation also clarifies the meaning of the correlation matrices shown in this chapter. The horizontal axis corresponds to the *interfering* channel—i.e., the channel whose power fluctuations induce nonlinear distortions— while the vertical axis corresponds to the *victim* channel being measured. Each matrix entry therefore quantifies the maximum nonlinear influence of one wavelength on another, independent of the relative walk–off imposed by chromatic dispersion.

The WDM dataset includes transmission distances of 80 km (0–12 dBm) and 120 km (12 dBm). The 80 km results illustrate how inter–channel nonlinearities evolve with launch power, while the 120 km case highlights the additional suppression produced by dispersion–induced walk–off.

5.2.1 Inter–Channel Cross-Phase Modulation (XPM)

Figures 11 and 12 show the peak XPM correlation matrices for victim polarizations x and y at 80 km, evaluated at 0, 4, 8, and 12 dBm. Each 4×4 matrix represents the correlation strength between each interferer–victim pair after full DSP compensation.

Three consistent behaviors emerge from the 80 km results:

- **0 dBm:** All correlations are $< 10^{-2}$, indicating essentially linear propagation.
- **4 and 8 dBm:** A clear increase in XPM is observed, especially between adjacent channels (C1–C2 and C3–C4), in agreement with classical predictions (AGRAWAL, 2019).
- **12 dBm:** Correlation values remain modest (< 0.06), well below intra–channel SPM levels.

Figures 13 and 14 show the associated peak–lag matrices. The dominant lags occur at non-zero offsets, reflecting the delay introduced by chromatic dispersion and confirming the walk-off-driven nature of XPM in coherent systems (DAR et al., 2014; MECOZZI; ESSIAMBRE, 2012).

The 120 km results at 12 dBm, shown in Figures 15 and 16, display the same qualitative structure, but with slightly reduced correlation amplitudes. The additional walk-off at this distance decreases temporal overlap between channels, weakening the deterministic component of XPM.

Overall, the XPM results indicate that inter-channel nonlinear coupling remains weak across both span lengths and does not challenge the dominance of intra-channel SPM in 400ZR-class short–reach links.

Figure 11 – Peak inter–channel XPM correlation matrices for victim polarization x over 80 km, evaluated at 0, 4, 8, and 12 dBm.

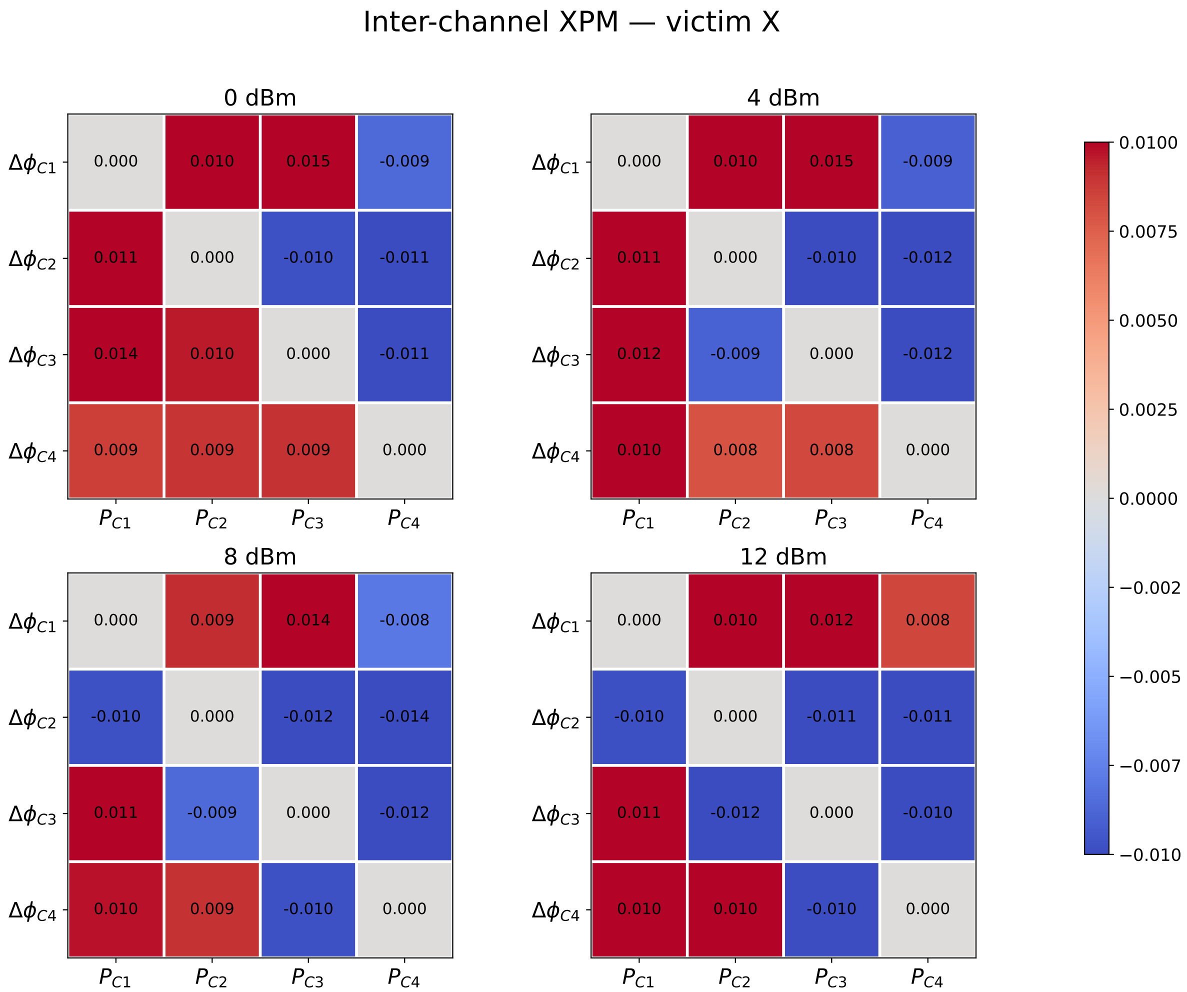

0 dBm	P_{C1}	P_{C2}	P_{C3}	P_{C4}
$\Delta\phi_{C1}$	0.000	0.010	0.015	-0.009
$\Delta\phi_{C2}$	0.011	0.000	-0.010	-0.011
$\Delta\phi_{C3}$	0.014	0.010	0.000	-0.011
$\Delta\phi_{C4}$	0.009	0.009	0.009	0.000

4 dBm	P_{C1}	P_{C2}	P_{C3}	P_{C4}
$\Delta\phi_{C1}$	0.000	0.010	0.015	-0.009
$\Delta\phi_{C2}$	0.011	0.000	-0.010	-0.012
$\Delta\phi_{C3}$	0.012	-0.009	0.000	-0.012
$\Delta\phi_{C4}$	0.010	0.008	0.008	0.000

8 dBm	P_{C1}	P_{C2}	P_{C3}	P_{C4}
$\Delta\phi_{C1}$	0.000	0.009	0.014	-0.008
$\Delta\phi_{C2}$	-0.010	0.000	-0.012	-0.014
$\Delta\phi_{C3}$	0.011	-0.009	0.000	-0.012
$\Delta\phi_{C4}$	0.010	0.009	-0.010	0.000

12 dBm	P_{C1}	P_{C2}	P_{C3}	P_{C4}
$\Delta\phi_{C1}$	0.000	0.010	0.012	0.008
$\Delta\phi_{C2}$	-0.010	0.000	-0.011	-0.011
$\Delta\phi_{C3}$	0.011	-0.012	0.000	-0.010
$\Delta\phi_{C4}$	0.010	0.010	-0.010	0.000

Source: Elaborated by the author.

5.2.2 Inter–channel Four-Wave Mixing (FWM)

Figures 17 and 18 present the FWM correlation matrices for the 80 km link at 12 dBm. The values are extremely small ($|\rho| < 3 \times 10^{-3}$), confirming strong suppression by chromatic dispersion and wide channel spacing (AGRAWAL, 2019).

At 120 km (Fig. 19 and Fig. 20), the additional dispersion further reduces the interaction, confirming that FWM plays no relevant role in the examined scenario.

FWM remains at least an order of magnitude weaker than XPM and several orders weaker than intra-channel SPM. Given the high dispersion and 75 GHz channel spacing of SSMF, phase matching is strongly impaired, resulting in negligible contributions to system performance. Thus, inter-channel FWM is not a limiting nonlinear impairment for the 400ZR configuration evaluated here.

Figure 12 – Peak inter–channel XPM correlation matrices for victim polarization y over 80 km, evaluated at 0, 4, 8, and 12 dBm.

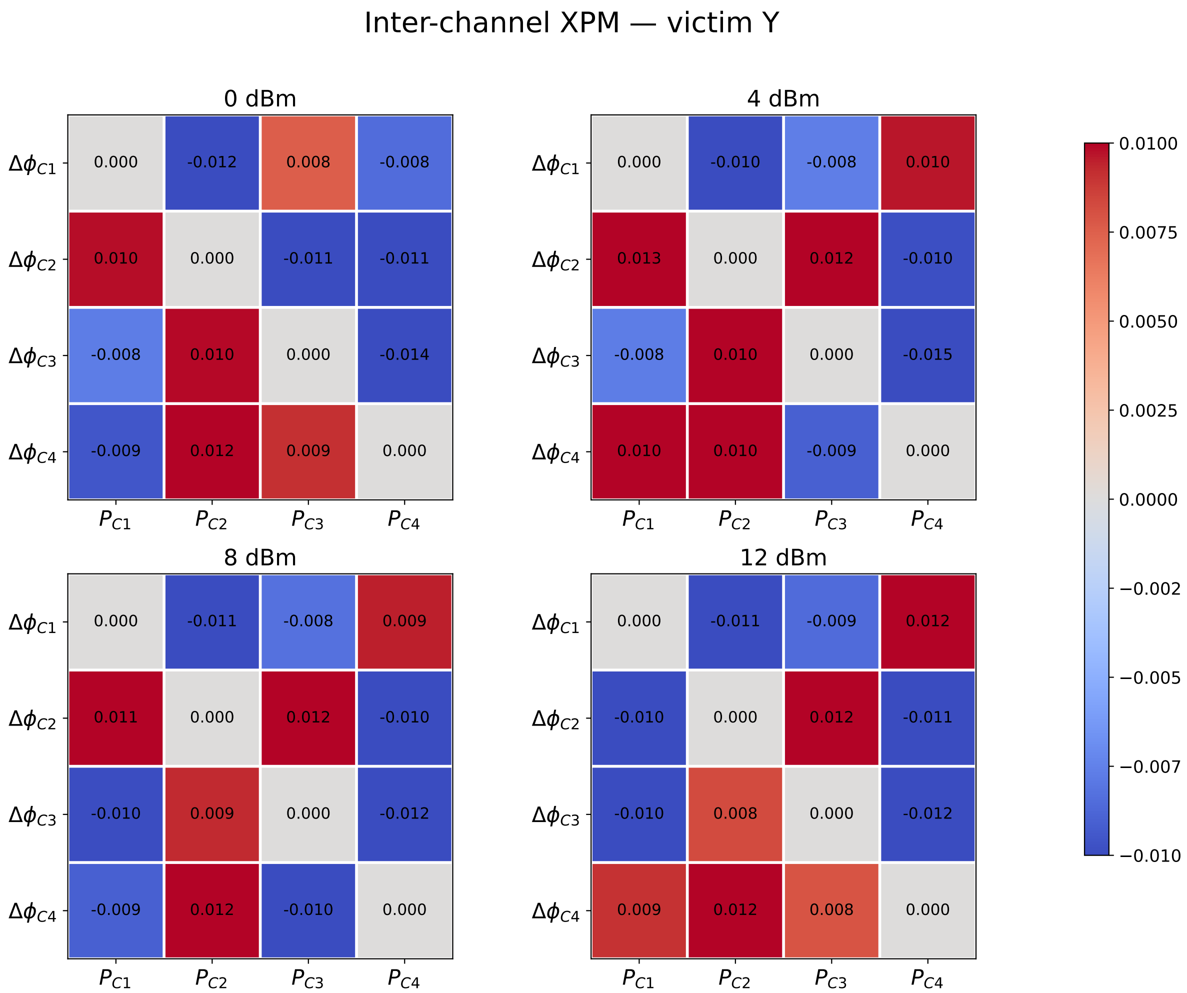

Source: Elaborated by the author.

Figure 13 – Peak-lag matrices for victim polarization x over 80 km, evaluated at 0, 4, 8, and 12 dBm.

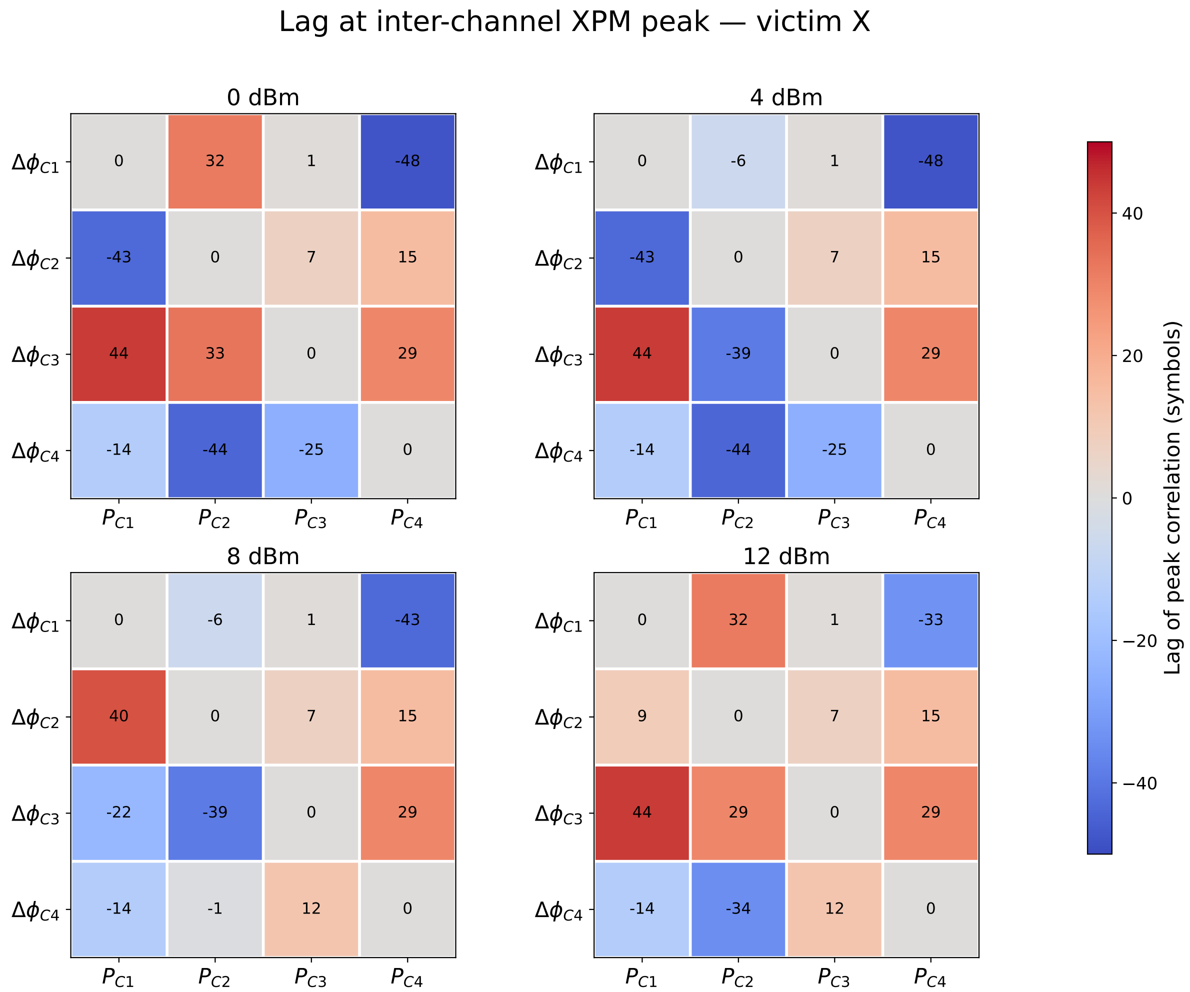

Source: Elaborated by the author.

Figure 14 – Peak-lag matrices for victim polarization y over 80 km, evaluated at 0, 4, 8, and 12 dBm.

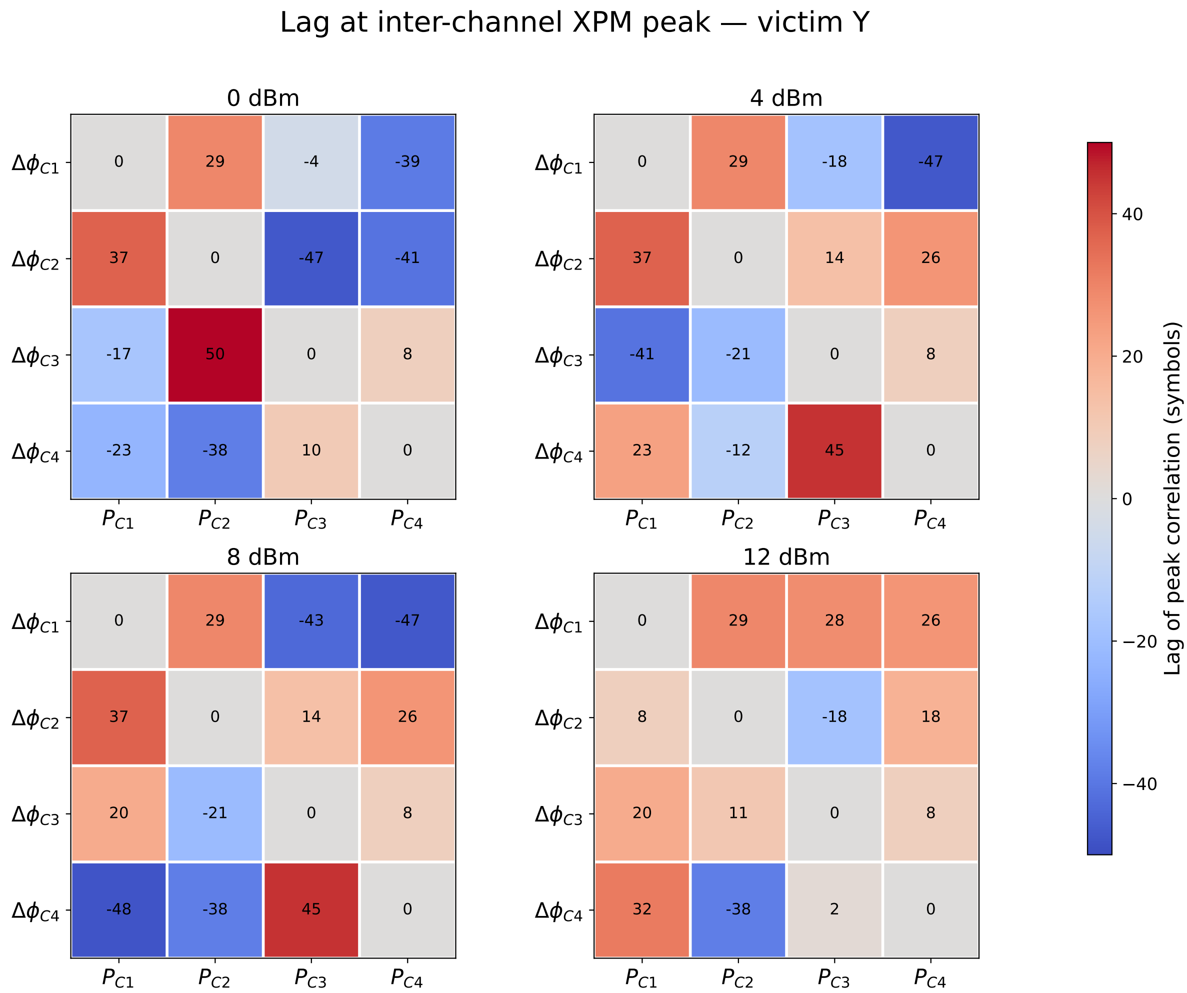

Source: Elaborated by the author.

Figure 15 – Inter–channel XPM correlation and peak-lag matrices for victim polarization x at 120 km and 12 dBm.

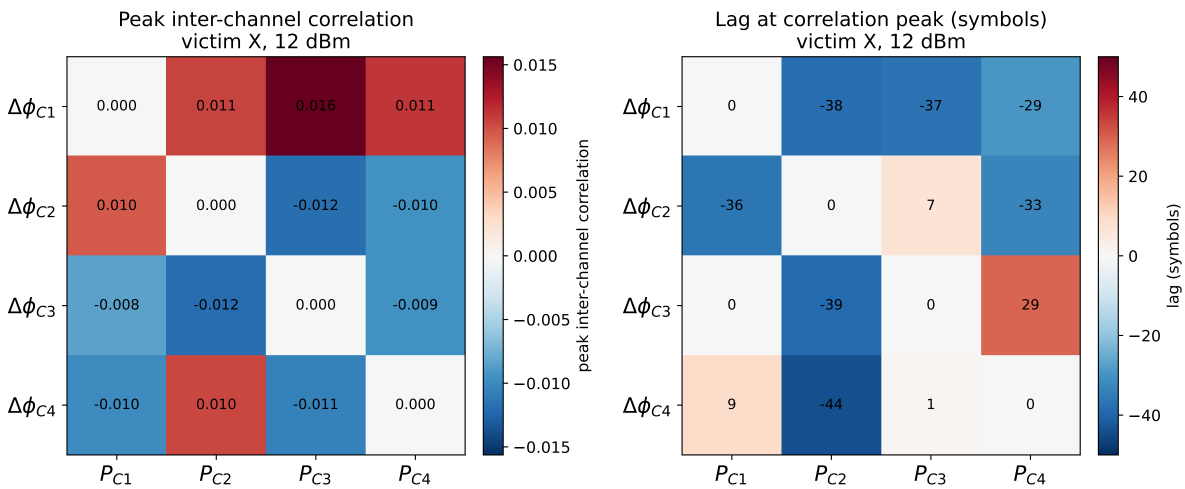

Source: Elaborated by the author.

Figure 16 – Inter–channel XPM correlation and peak-lag matrices for victim polarization y at 120 km and 12 dBm.

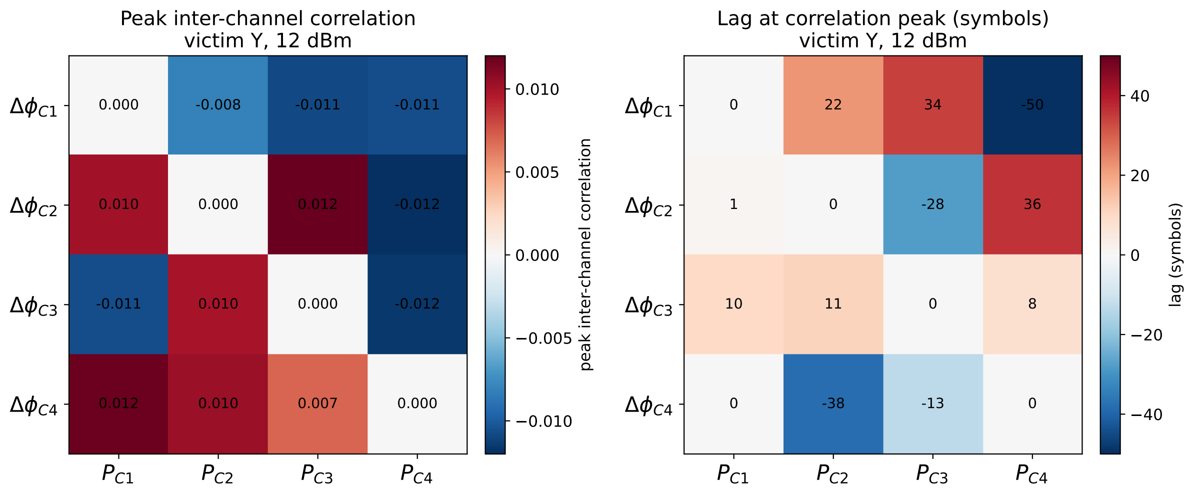

Source: Elaborated by the author.

Figure 17 – Inter-channel FWM correlation matrix for X polarization at 80 km and 12 dBm.

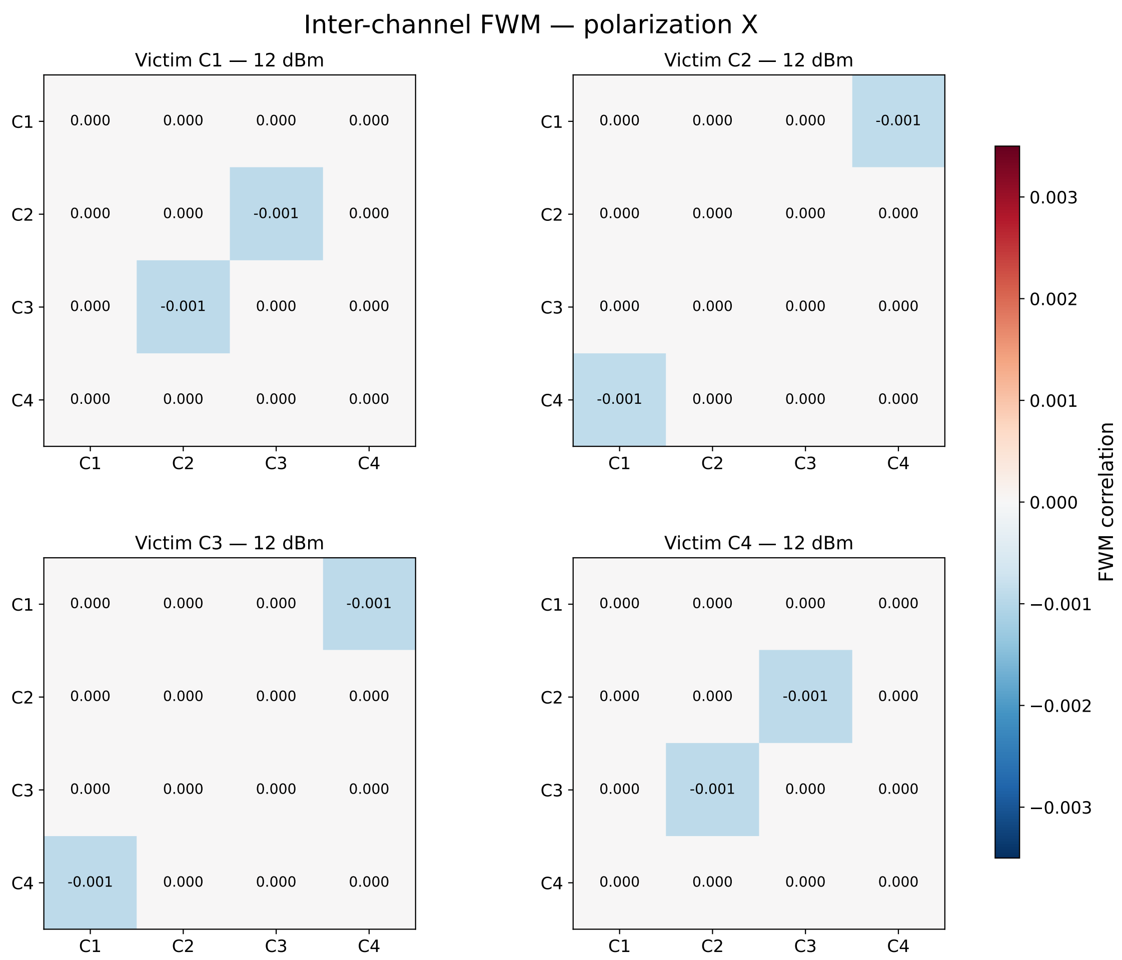

Source: Elaborated by the author.

Figure 18 – Inter-channel FWM correlation matrix for Y polarization at 80 km and 12 dBm.

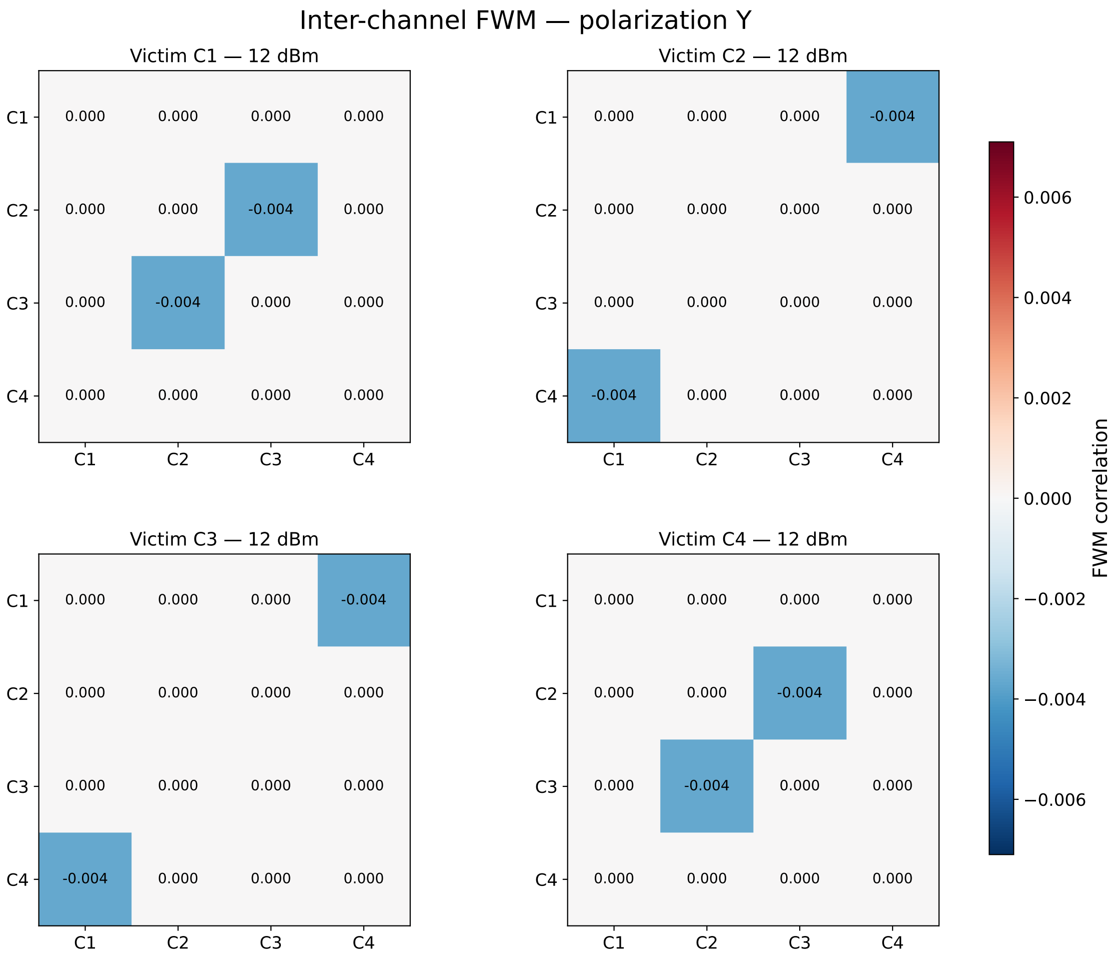

Source: Elaborated by the author.

Figure 19 – Inter-channel FWM correlation matrix for X polarization at 120 km and 12 dBm. Increased dispersion significantly suppresses FWM components.

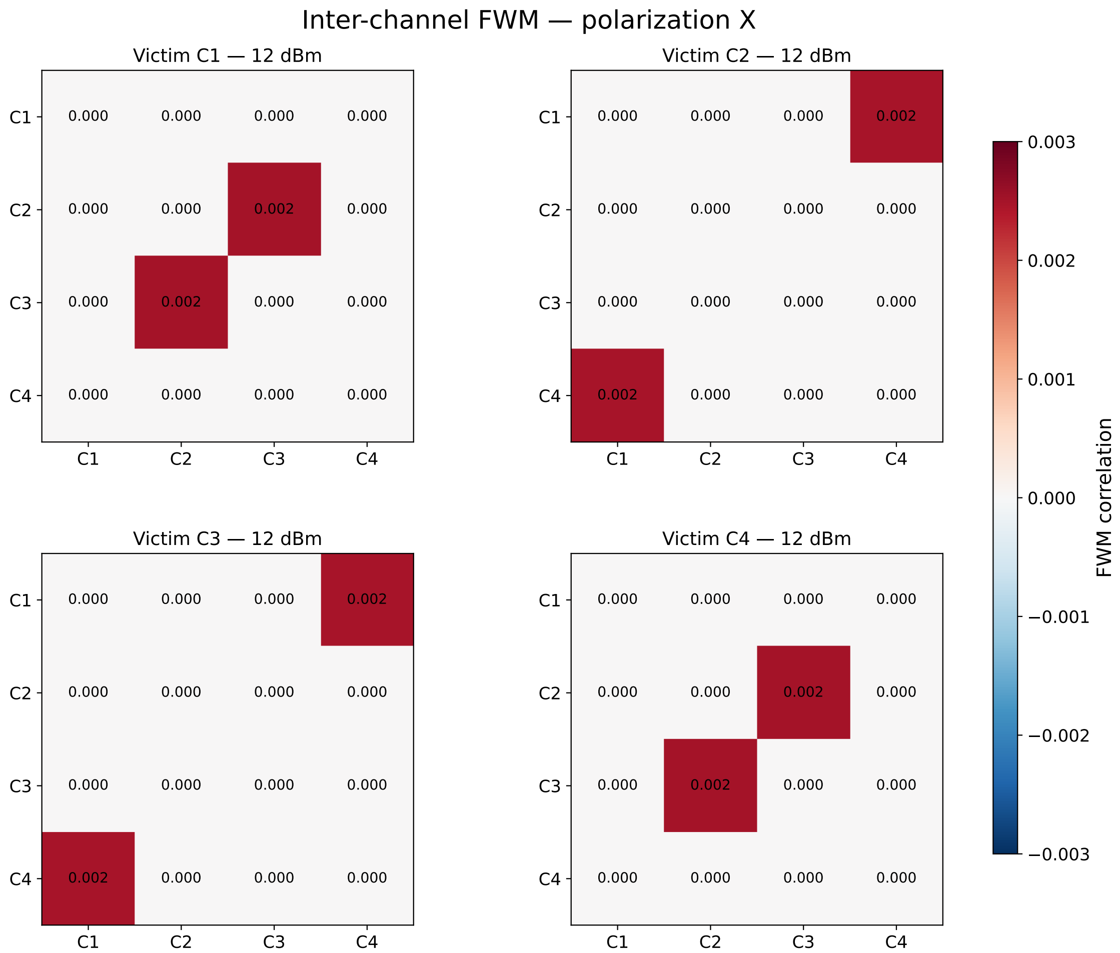

Source: Elaborated by the author.

Figure 20 – Inter-channel FWM correlation matrix for Y polarization at 120 km and 12 dBm. Increased dispersion significantly suppresses FWM components.

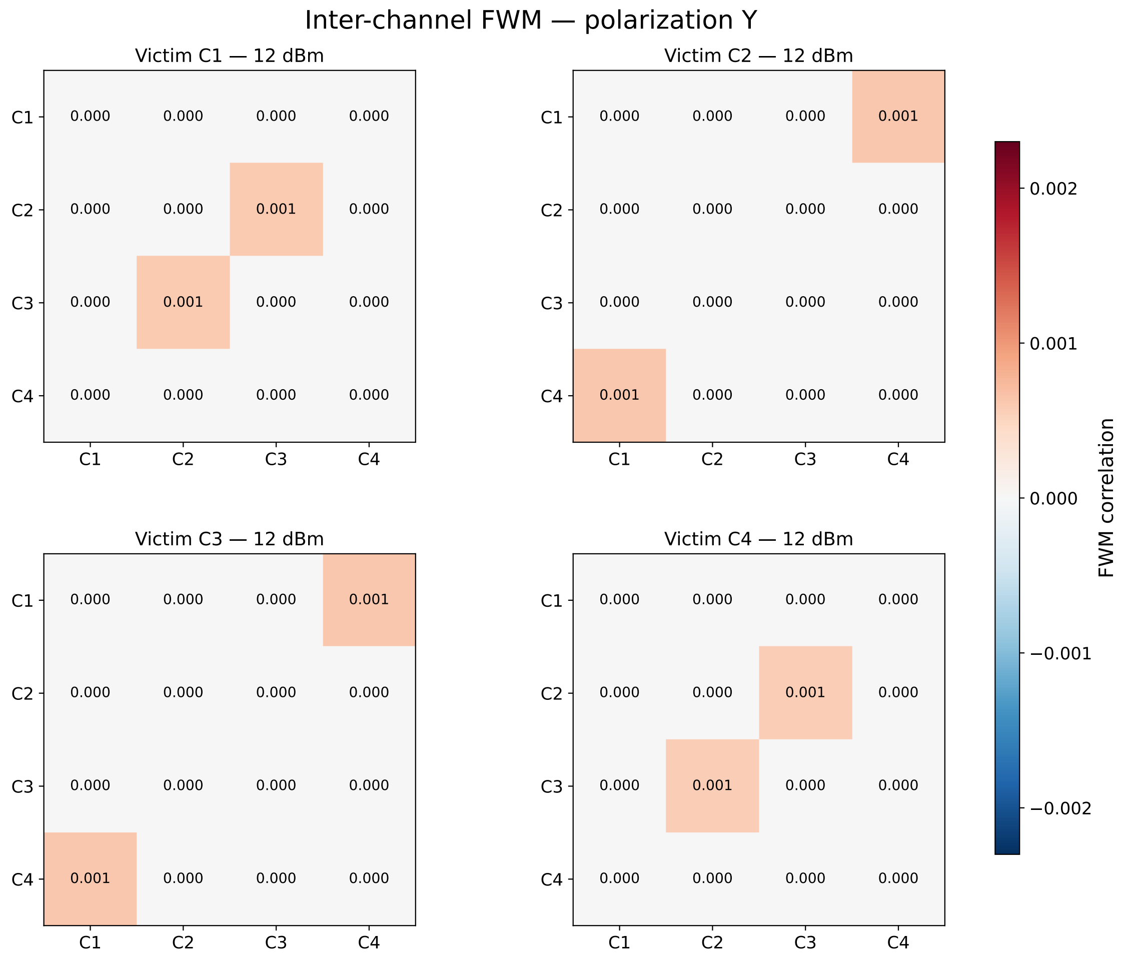

Source: Elaborated by the author.

6 CONCLUSIONS AND FUTURE WORK

This work developed a complete numerical framework for the analysis of nonlinear impairments in dual-polarization coherent transmission under 400ZR-class conditions. The methodology combined a commercial reference model (*VPItransmissionMaker*) with a fully transparent Python-based simulator, allowing both the validation of physical consistency and the detailed inspection of symbol-level effects that cannot be captured by traditional performance metrics.

6.1 CONCLUSIONS

Model validation. The Python coherent model was validated using the single-channel 80 km configuration. The close agreement with VPI across the entire launch-power range demonstrated that the numerical implementation correctly reproduces the main physical mechanisms affecting 400ZR transmission, including chromatic dispersion, ASE accumulation, and Kerr-induced effects. Once validated, the model was extended to multiple distances and to a four-channel WDM arrangement, providing a controlled environment for nonlinear analysis without the multi-channel artifacts present in the commercial tool.

Single-channel nonlinear behavior. For the 100 km case, nonlinear effects were evaluated using correlation-based metrics. The XPolM matrices indicated that both self-phase modulation and cross-polarization mixing remain extremely weak after the complete DSP chain, even at the highest studied launch powers. The results confirm that polarization orthogonality is preserved and that the dominant residual distortion behaves as stochastic phase noise rather than deterministic coupling.

Power-dependent nonlinear transition. Symbol-level diagnostics were used to complement the correlation analysis. By examining the residual phase error as a function of instantaneous power, it was possible to identify a clear transition between linear and nonlinear regimes. This visualization highlighted an intermediate operating region around 10–11 dBm, in which nonlinear distortions become detectable at the symbol level while remaining too weak to impact BER or correlation metrics. This transitional region reveals nonlinear propagation structures that precede measurable system penalties, showing the value of symbol-level inspection for coherent systems.

WDM nonlinear interactions. The multi-channel analysis showed that inter-channel effects remain modest for 400ZR-class operation. Cross-phase modulation becomes noticeable only at higher launch powers and is mainly limited to interactions between adjacent channels. Four-wave mixing exhibited negligible magnitude across all tested distances, strongly suppressed by chromatic dispersion and by the 75 GHz channel spacing. Together, these results indicate that deterministic nonlinear interactions play a secondary role under typical 400ZR operating conditions.

Overall conclusion. The combined analysis demonstrates that, although nonlinear effects are present, their deterministic components are significantly weakened by dispersion and are effectively mitigated by modern DSP. The dominant impairment is the stochastic phase noise associated with the Kerr effect, which cannot be fully revealed by traditional BER or EVM assessments. The use of both correlation-based and symbol-level tools proved essential for exposing nonlinear structures that would otherwise remain hidden. The methodology developed here thus provides a solid framework for deeper investigation of nonlinear propagation in coherent optical links.

6.2 FUTURE WORK

The methodology developed in this work opens several avenues for continued research:

- **Detailed analysis of the transitional power regime (10–11 dBm).** Further investigation is needed to characterize the mechanisms governing the onset of Kerr-induced distortions that precede measurable BER penalties.
- **Machine-learning-based NLI prediction.** The power–phase scatter distribution could serve as a feature map for learning models aimed at real-time estimation of nonlinear penalties.
- **Extension to denser WDM grids.** Evaluating 50 GHz or 37.5 GHz spacing would increase nonlinear coupling and reveal regimes where XPM and FWM become more relevant.
- **Higher-order modulation formats.** Formats such as 64-QAM and 256-QAM may exhibit stronger nonlinear signatures and richer correlation structures.
- **Experimental validation.** Applying the methodology to real 400ZR hardware traces would help validate the diagnostic tools under practical constraints.

The results of this work establish a solid foundation for advanced analysis of nonlinear impairments in coherent optical transmission and open the path toward more sophisticated diagnostic and predictive tools for future high-capacity networks.

BIBLIOGRAPHY

ADTRAN. **Coherent 400ZR Series**. 2025. Available at: <https://www.adtran.com/en/products-and-services/open-optical-networking/pluggables-and-subsystems/coherent-zr-series/coherent-400zr-series>.

AGRAWAL, G. P. **Nonlinear Fiber Optics**. 6. ed. San Diego, CA - USA: Academic Press, 2019.

CIENA. **WaveLogic 5 Nano 400ZR Transceiver Infobrief**. 2023. Available at: <https://www.psitec.com/assets/ciena/WaveLogic-5-Nano-400ZR-Transceiver-IB.pdf>.

CISCO. **Growing the Network with 400 Gbps Coherent Pluggable Optics**. 2022. Available at: <https://www.cisco.com/c/dam/en/us/solutions/collateral/service-provider/routed-optical-networking/white-paper-sp-400g-coherent-optics.pdf>.

CISCO. **400G Coherent Pluggable Optics Use Cases At a Glance. Technical Brief**. 2023. Available at: <https://www.cisco.com/c/en/us/products/collateral/interfaces-modules/transceiver-modules/nb-06-400g-coherent-pluggable-aag-cte-en.html>.

CISCO. **Coherent 400G Pluggable Optics aligned with 400ZR and OpenZR+ specifications. BRKOPT-2705 Presentation**. 2023. Available at: <https://www.ciscolive.com/c/dam/r/ciscolive/emea/docs/2023/pdf/BRKOPT-2705.pdf>.

DAR, R. et al. Properties of nonlinear noise in long, dispersion-uncompensated fiber links. **Optics Express**, v. 22, n. 12, p. 1503–1520, 2014.

FORUM, O. . I. **Implementation Agreement for 400ZR Interoperability Interface. OIF-400ZR-01.0**. 2020. Available at: <https://www.oiforum.com>.

FORUM, O. . I. **400ZR, OpenZR+, 800ZR Interoperability Demo – OFC 2024**. 2024. Available at: <https://www.oiforum.com/wp-content/uploads/OIF_400ZRplus_booth_slides_OFC2024-Final-1-1.pdf>.

FORUM, O. . I. **OIF 400ZR Interoperability White Paper — OFC 2025 Plugfest**. 2025. Available at: <https://www.oiforum.com/wp-content/uploads/OFC-2025-400ZR-White-Paper-4_17.pdf>.

IEEE. Ieee standard for ethernet amendment 5: Physical layer specifications and management parameters for 200 gb/s and 400 gb/s operation. ieee 802.3bs. **IEEE Standards**, 2017.

ITU-T. **Spectral grids for WDM applications: DWDM frequency grid. G.694.1**. 2012. Available at: <https://www.itu.int/rec/T-REC-G.694.1/en>.

KEISER, G. **Optical Fiber Communications**. 5. ed. New York, NY - USA: McGraw-Hill, 2021.

MECOZZI, A.; ESSIAMBRE, R. Nonlinear shannon limit in pseudo-linear coherent systems. **Journal of Lightwave Technology**, v. 30, n. 12, p. 2011–2024, 2012.

MSA, O. **OpenZR+ White Paper**. 2023. Available at: <https://openzrplus.org/wp-content/uploads/2024/04/openzrplus_whitepaper_rev0_92_2023-12-19_final.pdf>.

NETO, E. L.; ALDAYA, I. et al. Dsp-based impairment compensation in coherent optical systems. **Journal of Lightwave Technology**, v. 38, n. 18, p. 4930–4945, 2020.

OPTICS, I. **Boost Your Bandwidth 400ZR and OpenZR+!** 2024. Available at: <https://integraoptics.com/boost-your-bandwidth-400zr-and-open-zr/>.

POGGIOLINI, M. The gn model of nonlinear propagation in uncompensated coherent optical systems. **Journal of Lightwave Technology**, v. 30, n. 24, p. 3857–3879, 2012.

SAVORY, S. J. Digital filters for coherent optical receivers. **Optics Express**, v. 16, n. 2, p. 804–817, 2008.

SAVORY, S. J. Digital coherent optical receivers: Algorithms and subsystems. In: **OFC/NFOEC 2012**. [S.l.: s.n.], 2012.

ZHAO, J.; LIU, Y.; XU, T. Advanced dsp for coherent optical fiber communication. **Applied Sciences**, v. 9, n. 20, p. 4190, 2019.

APPENDIX A – DSP IN COHERENT SYSTEMS

Digital coherent optical systems rely heavily on advanced signal processing to recover the transmitted information from distorted and noise-impaired optical signals. The DSP unit in the receiver compensates for various transmission impairments, including chromatic dispersion, PMD, frequency offset, and phase noise. These effects arise due to the interaction between the optical carrier, fiber transmission medium, and local oscillators, and their joint mitigation is crucial for achieving reliable data recovery in high-capacity systems such as the 400ZR standard.

Figure 21 – Generic digital coherent optical transmission system illustrating the main physical impairments compensated by DSP algorithms.

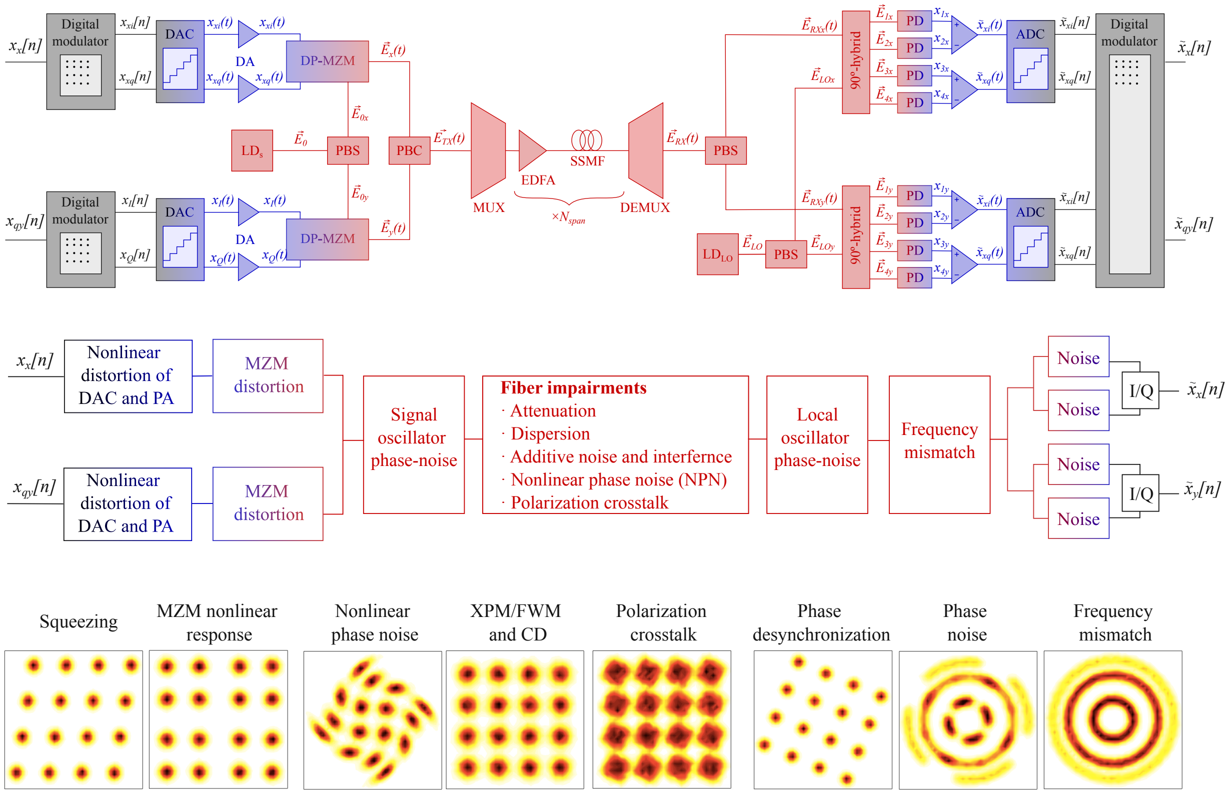

Source: Elaborated by the author.

As shown in Fig. 21, a coherent transceiver consists of a digital transmitter, an optical front-end, a transmission link, and a coherent receiver followed by a DSP chain. Throughout propagation, several impairments accumulate: CD broadens optical pulses temporally; PMD causes differential delays between orthogonal polarization components; nonlinear effects such as SPM and XPM induce phase noise and inter-symbol interference; while frequency offset and phase noise arise from the finite linewidths of the transmitter and local oscillator lasers.

The digital receiver is responsible for compensating these effects, restoring the orthogonality between polarizations and recovering the transmitted constellation. The following sections describe the main DSP stages typically employed in coherent receivers—chromatic dispersion compensation, PMD equalization, CFO correction, and carrier phase recovery—highlighting their theoretical basis and functional role in 400ZR-like systems.

A.1 CHROMATIC DISPERSION COMPENSATION

Chromatic dispersion (CD) is one of the most significant linear impairments in coherent optical transmission. It originates from the wavelength dependence of the group velocity in the optical fiber, causing different frequency components of a signal to propagate at different speeds. As a result, optical pulses broaden as they travel along the fiber, leading to inter-symbol interference (ISI) that degrades the received signal quality.

In the frequency domain, the transfer function of the fiber due to chromatic dispersion can be expressed as

$$H_{\mathrm{CD}}(f) = \exp\big(-j\pi D\lambda^2 L f^2/c\big), \tag{18}$$

where D is the chromatic dispersion parameter (typically 17 ps/nm/km for standard single-mode fiber at 1550 nm), λ is the central wavelength, L is the transmission distance, f is the frequency offset relative to the optical carrier, and c is the speed of light in vacuum (AGRAWAL, 2019).

In digital coherent receivers, chromatic dispersion can be fully compensated by applying an inverse filter that restores the original phase relationship among frequency components. The compensation filter is given by

$$H_{\mathrm{EQ}}(f) = \exp\big(j\pi D\lambda^2 L f^2/c\big). \tag{19}$$

This operation can be efficiently implemented in the frequency domain using the fast Fourier transform (FFT) and its inverse (IFFT), forming the so-called *frequency-domain equalizer* (FDE). The computational complexity of FDE-based dispersion compensation scales as $\mathcal{O}(N \log N)$, making it particularly suitable for high-baudrate systems such as 400ZR, which employ symbol rates up to 64 Gbaud (SAVORY, 2008; ZHAO; LIU; XU, 2019).

An alternative time-domain approach, known as finite impulse response (FIR) filtering, may also be used when the accumulated dispersion is moderate. However, for long-haul or dispersion-uncompensated links, the number of required taps becomes prohibitively large. Therefore, 400ZR-class transceivers adopt FDE implementations, which can handle accumulated dispersions exceeding 10,000 ps/nm with acceptable hardware complexity.

The chromatic dispersion equalization stage is typically one of the first processing blocks applied to the digitized signal, preceding adaptive polarization demultiplexing. Once CD is compensated, the signal becomes temporally aligned, allowing subsequent DSP modules to efficiently correct polarization and phase distortions.

A.2 POLARIZATION DEMULTIPLEXING AND PMD COMPENSATION

In DP coherent transmission, two orthogonal polarization components, typically denoted as x and y, are independently modulated to double the system's spectral efficiency. Although both polarizations propagate simultaneously through the same optical fiber, birefringence and external perturbations—such as mechanical stress, temperature fluctuations, and microbending—introduce random coupling between them. This phenomenon, known as PMD, leads to differential group delay (DGD) and polarization-dependent fading, both of which significantly degrade the received signal quality (SAVORY, 2008; ZHAO; LIU; XU, 2019).

Figure 22 – Illustration of Polarization Mode Dispersion (PMD) in an optical fiber, showing differential group delay between orthogonal polarization components.

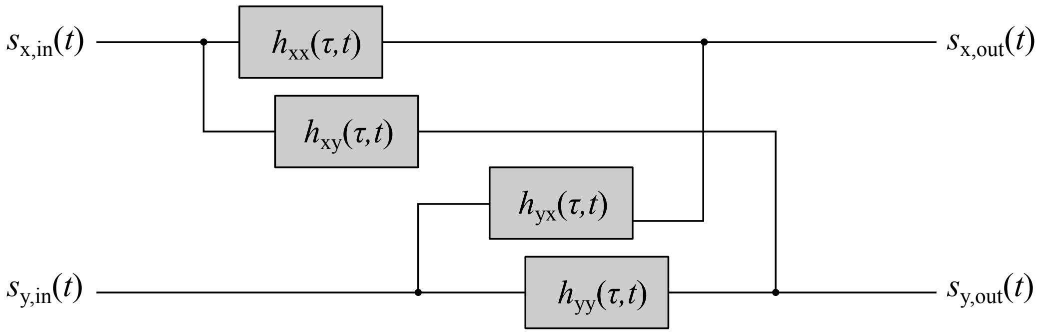

Source: Elaborated by the author.

In the linear propagation regime, the evolution of the optical field along the fiber can be represented as a two-dimensional system:

$$\begin{bmatrix} A'_x(z) \\ A'_y(z) \end{bmatrix} = \mathbf{H}(z) \begin{bmatrix} A_x(z) \\ A_y(z) \end{bmatrix}, \tag{20}$$

where $\mathbf{H}(z)$ is a complex 2×2 transfer matrix describing the polarization coupling and differential delay induced by PMD. The matrix $\mathbf{H}(z)$ varies stochastically along the fiber length and in time, making static optical compensation impractical in real systems. Therefore, compensation is carried out digitally using adaptive MIMO equalization implemented in the receiver DSP (SAVORY, 2012).

The most common MIMO equalizer structure for 400ZR-class transceivers is the 2×2 butterfly filter, whose operation can be expressed as:

$$\begin{bmatrix} \hat{A}_x \\ \hat{A}_y \end{bmatrix} = \begin{bmatrix} F_{xx}(z) & F_{xy}(z) \\ F_{yx}(z) & F_{yy}(z) \end{bmatrix} * \begin{bmatrix} A'_x(z) \\ A'_y(z) \end{bmatrix}, \tag{21}$$

where the symbol $*$ denotes convolution, and each coefficient $F_{ij}(z)$ represents a FIR filter that dynamically compensates both the polarization rotation and the differential delay between the two channels.

Figure 23 – Digital compensation of PMD in the receiver through adaptive polarization demultiplexing using MIMO equalization.

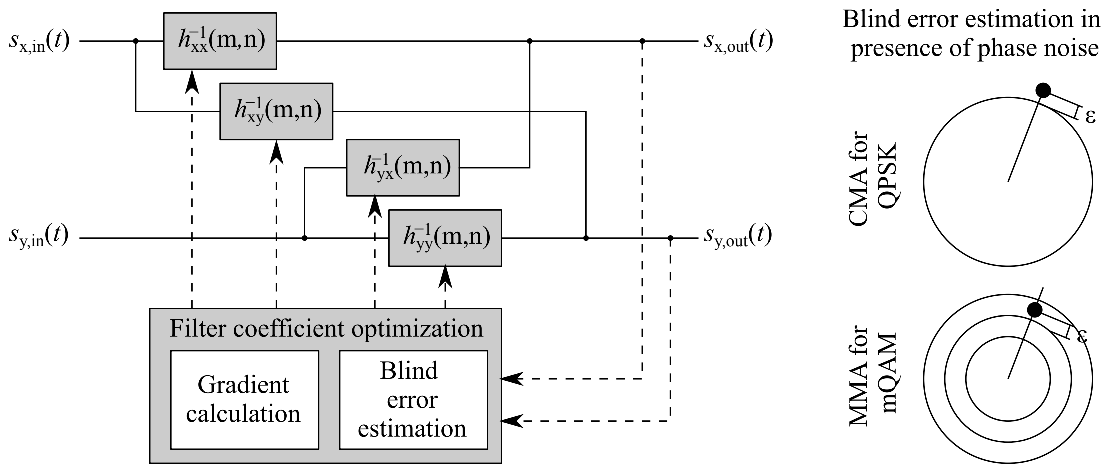

Source: Elaborated by the author.

The adaptive coefficients of the MIMO equalizer are continuously updated using algorithms such as Least Mean Squares (LMS) or Constant Modulus Algorithm (CMA), depending on the modulation format and convergence requirements. For high-order modulation formats, such as DP-16QAM used in 400ZR, decision-directed schemes like the are often preferred, as they exploit prior constellation knowledge to improve convergence and stability (ZHAO; LIU; XU, 2019).

The MIMO equalizer thus performs two main tasks: (i) compensating for the PMD-induced temporal misalignment between the two polarization tributaries, and (ii) correcting random polarization rotations caused by time-varying birefringence in the transmission fiber. In 400ZR systems operating at 64 Gbaud, the DSP must adapt rapidly—on time scales of milliseconds—to ensure continuous orthogonality between the recovered x and y components. Once polarization demultiplexing and PMD compensation are achieved, subsequent DSP stages execute CFO correction and to fully reconstruct the transmitted symbols.

A.3 CARRIER RECOVERY

In coherent optical receivers, the recovery of the carrier is a crucial stage of DSP. It compensates for frequency and phase mismatches between the transmitter and local oscillator (LO) lasers. Without this step, the constellations of quadrature-modulated signals such as DP-QPSK or DP-16QAM would rotate over time, preventing proper symbol demodulation (**??**KEISER, 2021).

A.3.1 Carrier Frequency Offset

Due to the independent nature of the transmitter and receiver lasers, their optical frequencies are never perfectly identical. If the transmitter operates at frequency ω_T and the local oscillator at ω_{LO}, the detected signal experiences a frequency offset given by

$$\Delta\omega = \omega_T - \omega_{LO}. \tag{22}$$

This CFO manifests as a continuous rotation of the baseband constellation, which can be expressed as

$$r(t) = s(t)e^{j2\pi\Delta f t}, \tag{23}$$

where $\Delta f = \frac{\Delta\omega}{2\pi}$ and $r(t)$ represents the received complex envelope. The result is a progressive phase rotation in the complex plane that depends linearly on time, as illustrated in Fig. 24.

Figure 24 – Effect of frequency offset on a 16-QAM constellation: (a) without frequency offset, and (b) with frequency offset, showing the continuous rotation of the symbols.

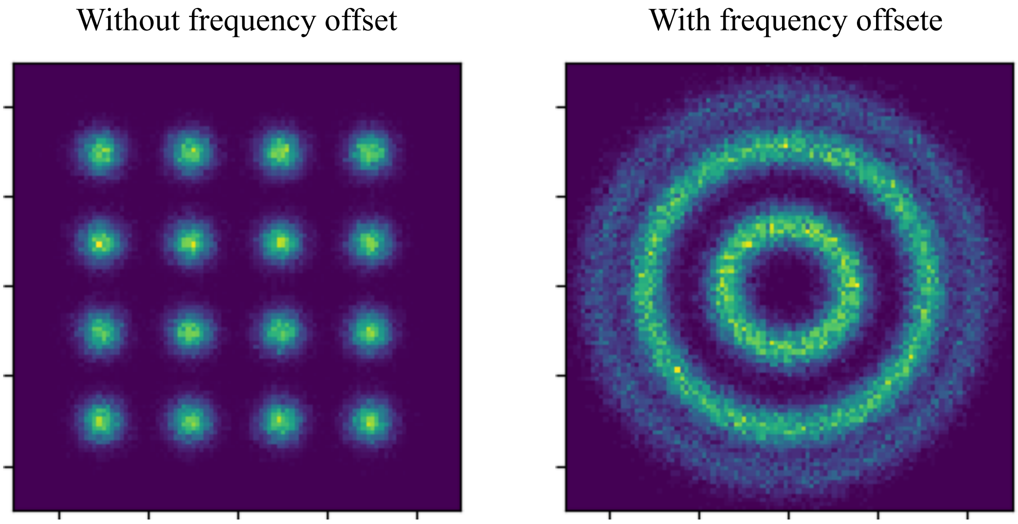

Source: Elaborated by the author.

In practice, the CFO originates from small frequency differences between the transmitter and LO lasers, as well as from slow thermal drifts. Typical offsets in 400ZR-class coherent systems are on the order of a few megahertz, while phase noise fluctuations act at much lower frequencies (kilohertz range).

To correct for the CFO, the DSP estimates $\hat{\Delta f}$ and applies the inverse rotation:

$$\hat{s}(t) = r(t)e^{-j2\pi\hat{\Delta f}t}. \tag{24}$$

This operation compensates the constant frequency mismatch and stabilizes the constellation before phase noise correction.

A.3.2 Carrier Phase Recovery

After the CFO compensation, residual phase fluctuations remain due to the finite linewidth of the transmitter and LO lasers. These fast, stochastic phase variations cause random rotations of the constellation and must be mitigated by *Carrier Phase Recovery* (CPR).

Figure 25 – Effect of phase noise on a 16-QAM constellation: (a) without phase noise, and (b) with phase noise, showing random fluctuations in symbol position.

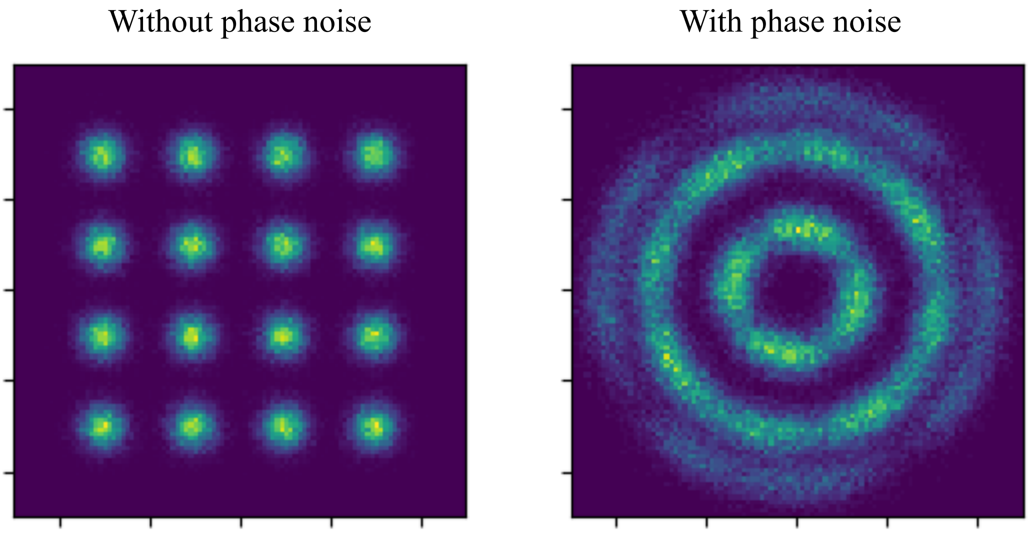

Source: Elaborated by the author.

CPR algorithms estimate and remove the instantaneous phase noise from the signal. Among the most common approaches are:

- The **Viterbi–Viterbi** algorithm, typically used in QPSK systems, which relies on the symmetry of the constellation to estimate the common phase.
- The **Blind Phase Search** (BPS) algorithm, widely adopted for higher-order QAM formats such as 16QAM, which tests a set of candidate phase rotations and selects the one minimizing the decision error (**??**).

The combined action of CFO and CPR blocks restores the complex symbols to their correct phase alignment, allowing symbol demapping and decoding to proceed without rotation-induced errors.

In the 400ZR standard, where DP-16QAM operates at 64 Gbaud, the precision of the carrier recovery process is essential to maintain low EVM and achieve the required BER performance.